THE PROPAGATION OF ELECTROMAGNETIC WAVES THROUGH STRATIFIED TERRESTRIAL MEDIA

By

STEVEN MICHAEL SHOPE

Bachelor of Arts

Lycoming College

Williamsport, Pennsylvania

1978

Submitted to the Faculty of the Graduate College
of the Oklahoma State University
in partial fulfillment of the requirements
for the Degree of
MASTER OF SCIENCE
December, 1978

THE PROPAGATION OF ELECTROMAGNETIC WAVES THROUGH

STRATIFIED TERRESTRIAL MEDIA

Thesis Approved:

James Lang
Thesis Adviser

Hugh L Smith

Jack J Martin

Norman N Hackman
Dean of the Graduate College

ACKNOWLEDGMENTS

The author wishes to express sincere appreciation to his major adviser, Dr. James Lange, for his interest, assistance and guidance throughout the course of this research and the master's program.

Additional thanks is extended to Dr. Gary Stewart, Department of Geology, for his important contributions to this research. Also, gratitude is extended to Dr. J. Martin and Dr. H. Scott for serving on my Master's Committee.

The Physics-Chemistry Machine Shop was instrumental in the construction of a large part of the experimental apparatus. Appreciation is extended to Heinz Hall for much advice and encouragement. A note of thanks to Janet Sallee for her fine typing of the manuscript.

Special thanks is given to my mother, and to Laura for their continued help and encouragement.

TABLE OF CONTENTS

LIST OF TABLES

LIST OF FIGURES

CHAPTER I

INTRODUCTION

The term geophysical exploration is traditionally associated with the industrial exploitation of economically feasible natural resources contained within the earth. Specifically it has to do with the location and identification of such resources or resource bearing formation. A general group of exploration methods is termed the remote sensing type, this infers that the exploration for objectives located beneath the surface is carried out from ground level or the air. There are numerous geophysical remote sensing prospecting methods available, usually each having been developed with a particular objective in mind, examples include magnetometers, gravitometers, resistivities, seismography, etc. Most of these devices operate by locating anomalies of various parameters associated with each geologic area.

Due to the necessity of petroleum to this century's technological growth, petroleum has been a financially attractive resource to exploit. Not unexpectedly, seismography, the chief exploration method for mapping the subsurface formations associated with petroleum, has seen comprehensive use and unprecedented development among exploration devices since its conception in 1919 (23). The seismograph is the only remote sensing device that can actually profile the strata located in the subsurface. Figure 1 is a typical seismograph recording while Figure 2 depicts the appearance of strata in the subsurface associated with

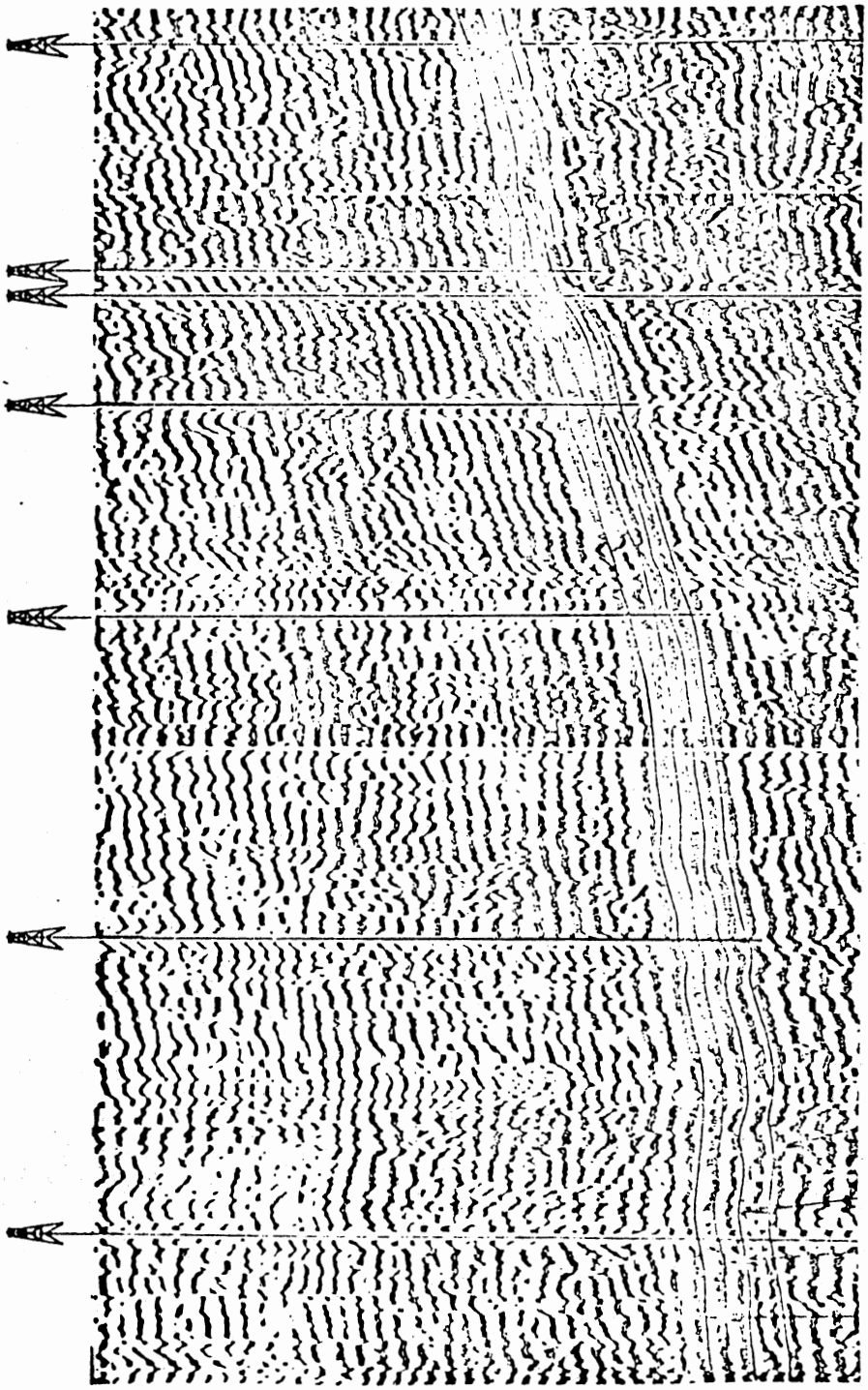

Figure 1. Typical Seismograph Data

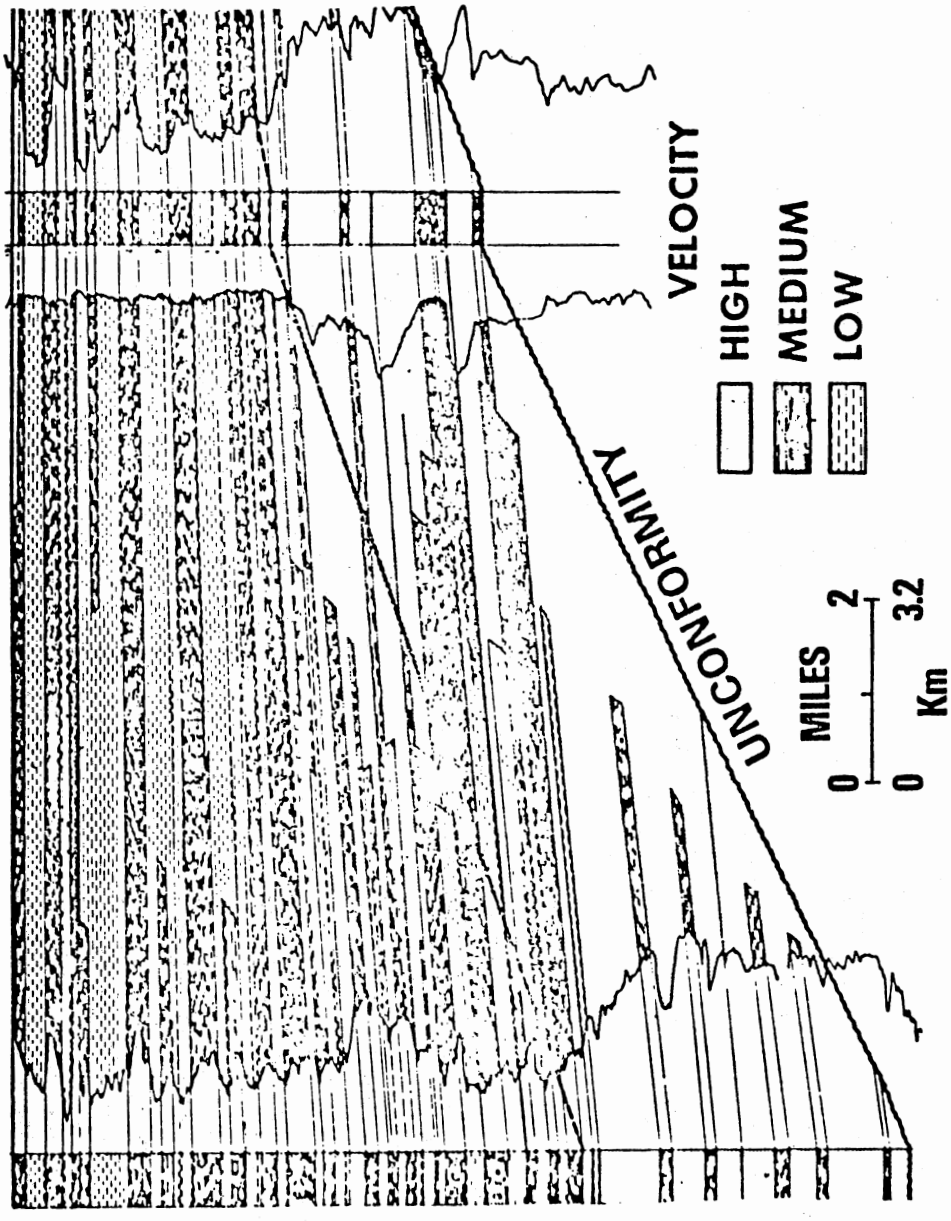

Figure 2. Strata Cross Section as Interpreted From Figure 1

the seismogram.

Briefly, a seismograph employs the propagation of longitudinal and transverse acoustical waves into the earth and by a variety of detector arrays, detects the reflection of these waves in a time domain system. The reflection of these waves occur at an interface of two strata possessing different acoustical impedances, where the impedance is the product of the density and wave's velocity. Emperically it has been found that the practical acoustical bandwidth of seismography is from 10 hz to approximately 300 hz. At higher frequencies massive scattering and loss of penetration occur, possibly due to the steepness of the dispersion curve. This low frequency operating range limits the resolution to the order of hundreds of feet. Since the large hydrocarbon reserves are associated with formations of this size, and because the reserves are usually thousands of feet underground, seismography has enjoyed considerable success.

However, a detailed remote sensing profile of the shallow subsurface, shallow referring to within several hundred feet of the surface, by means of seismography, is useless due to the deficiency of resolution. Until recently this posed no problem since it was much more accurate to simply drill core samples which would provide a direct physical profile of the subsurface. Presently, due to the expense of coring, the number of samples that may be economically taken is decreasing, hence the accuracy of a subsurface profile is reduced. In addition, environmental regulations, time, terrain and unexcessable locations such as mines necessitate the development of an alternate to coring, capable of an accurate surface profile.

In spite of the large industrial effort to develop a high frequency

seismograph (> 300 hz), experiment shows only the largest of shallow subsurface discontinuities could be detected by acoustical means. Consequently, a solution to the problem may be the use of high frequency electromagnetic waves in analogy to the use of acoustical waves in seismography.

Synonymous with the reflections that occur with acoustical waves, an electromagnetic wave will be reflected from stratum possessing a different electrical impedance. Using a time domain receive system in conjunction with various antenna arrays, a subsurface profile may be constructed. In order to obtain a resolution of one or two feet in a time domain system, a pulsed rf system would have to be used with a pulse of the order of one nanosecond in length. Since generating a pulse of this length from a monochromatic wave would be difficult and would contain a broad spectrum of fourier harmonics, it would be more advantageous to create a voltage impulse of this length in a gaussian shape. This would result in the frequency spectrum of the impulse appearing as a gaussian also.

The use of a broadband system has its advantages over a monochromatic wave in that due to the complex dispersion characteristics of some materials, the propagation of a monochromatic wave through a complexion of materials may result in the wave being highly attenuated, whereas the propagation of a large band of frequencies through a complexion has a larger probability that there will be components that will experience little attenuation. None the less, the voltage impulse will have to be of a moderately high power level, not only to overcome any attenuation present, but also since the amplitude of a reflection in a multilayered complexion will be very small resulting from the in-

ternal reflection and transmission coefficients.

It is possible that the received pulse may be distorted by any dispersion present, however, by convoluting the incident and received pulse the dispersion curve may be determined, which may aid in the identification of the material.

The intention of this thesis is not to develop or design an operational subsurface reflectometer, but to investigate the problem of the propagation of an electromagnetic pulse through a complexion of terrestrial materials. Specifically, this study will be concerned with a complexion consisting of layered media and with the propagation analysis of the electric field component of the electromagnetic pulse. Each medium may be macroscopically homogenous or nonhomogenous and may possess dissipation and/or complex dispersion. Whether such a subsurface reflectometer would ever be practical depends largely on the high frequency propagational characteristics of terrestrial materials.

In order to do this a reflectometer was constructed in the laboratory and sample dielectric layers introduced to it. This was accomplished by utilizing an impulse source and coaxial waveguides. By analysis of the reflected pulse amplitude and/or the time of flight between reflections, the dielectric constant of each material could be determined if the layer thickness is known. However, in an unguided system, the layer thickness need not be known since this information could be obtained by the use of incidences other than normal.

CHAPTER II

MATHEMATICAL DERIVATIONS

Electromagnetic Wave Propagation

Although the greater part of this study concerns itself with the propagation of electromagnetic waves in a coaxial waveguide, it is appropriate to discuss some of the general aspects of unguided waves first, with emphasis on the reflection and transmission process in a complexion of dissimilar dielectrics. The characteristics equation of the coaxial waveguide is then derived so that the field configurations inside the waveguide may be determined. Also, in order to obtain the frequency spectrum of the impulse, it is curve fitted in time and fourier transformed to the frequency domain.

The logical place to begin when discussing electromagnetic radiation is the four equations of Maxwell; in an absence of sources these four equations completely describe the transportation of energy from one point to another;

$$\vec{\nabla} \cdot \vec{B} = 0$$

$$\vec{\nabla} \cdot \vec{E} = 0$$

$$\vec{\nabla} \times \vec{E} = -\frac{1}{c} \frac{d\vec{B}}{dt}$$

$$\vec{\nabla} \times \vec{B} = \frac{\mu \epsilon_r}{c} \frac{d\vec{E}}{dt}$$

where the electrical (magnetic) parameters of the medium are completely

described by ε_r and μ, both of which may be complex quantities and/or functions of frequency. By the curl of the second equation and virtue of the first, the well known scalar wave equation for each component of $\vec{E}$ may be derived;

$$\nabla^2 E - \frac{1}{v^2} \frac{d^2 E}{dt^2} = 0$$

where v is the velocity of propagation;

$$v = \frac{c}{\sqrt{\mu \varepsilon_r}}$$

In a similar manner, the magnetic field components of $\vec{B}$ may be derived, but for the greater part of this chapter only the electric field components will be of interest.

Solutions to the scalar wave equation of the second order are;

$$E = E_o e^{i\vec{k}\cdot\vec{r} - i\omega t}$$

These are the well known plane wave equations, where the quantity $\vec{k}$ is the wave vector in the direction of the flow of energy. For instance at any point z in space, the magnitude of a wave propagating in the $\vec{z}$ direction is;

$$\vec{E} = E_x \hat{i} + E_y \hat{j} = (E_{ox} \hat{i} + E_{oy} \hat{j} + E_{oz} \hat{k})\, e^{i\vec{k}\cdot\vec{z} - i\omega t}$$

This wave is plane polarized in the x-y plane. Obviously E_{oz} can have no z time dependence. The wave vector $\vec{k}$ has a magnitude of;

$$\frac{\omega}{v} = \frac{\sqrt{\mu \varepsilon_r}\, \omega}{c} .$$

It must be remembered that $|\vec{k}|$ may be complex since μ and ε_r may be

complex functions. For the remainder of this discussion μ may be assumed to be real and for most terrestrial materials it has a magnitude of unity in Gaussian units.

The complex function, ε_r may conveniently be divided into its real and imaginary parts, assuming an Ohms law type behavior, such as;

$$\varepsilon_r = \text{Re } \varepsilon_r + \text{Im } \varepsilon_r = \varepsilon_r + \frac{i4\pi\sigma}{\omega}$$

where σ is known as the conductivity and represents dissipation of energy from the wave to the medium and Re ε_r represents the storage of energy by the medium. In terms of the real and imaginary parts of the dielectric constant, the complex wave number is;

$$k^2 = \mu\varepsilon_r \frac{\omega^2}{c^2} \left(1 + \frac{i4\pi\sigma}{\omega\varepsilon_r}\right)$$

with the branch;

$$k = \frac{\sqrt{\varepsilon_r}\,\omega}{c} + \frac{i\alpha}{2}$$

where α is known as the attenuation coefficient. In terms of the conductivity, σ for good conductors ($\frac{4\pi\sigma}{\omega\varepsilon_r} >> 1$) is;

$$\alpha = \frac{2\sqrt{2\pi\omega\sigma}}{c}$$

When α is greater than zero, the wave is attenuated in amplitude as $e^{-\alpha x}$. For example, if the field strength falls from E_1 to E_2 after after passing through x meters of a lossy medium, then the attenuation coefficient is;

$$\alpha = \frac{20 \ln (E_1/E_2)}{x} \left[\frac{\text{nepers}}{\text{m}}\right]$$

The presence of an electrical discontinuity in the space of the propagating wave denotes a boundary which interacts with the wave incident upon it. By means of the boundary conditions in conjunction with the continuity of $\vec{D}$ and $\vec{E}$, the laws of reflection and refraction follow. These laws can be divided into two parts; 1) where the $\vec{E}$ field is perpendicular to the plane of incidence and 2) where the $\vec{E}$ field is parallel to the plane of incidence. The symbols R for the reflection coefficient and T for the transmission coefficient are utilized in the following description. Consider a wave incident to the interface at an angle θ, where θ is the angle between $\vec{k}$, and the normal to the interface, $\hat{n}$. The incident wave is traveling in a medium of refractive index n (where $n = \sqrt{\mu\varepsilon_r}$) and incident upon a medium of refractive index n' ($n'=\sqrt{\mu'\varepsilon'_r}$). The coefficients for the two cases are as follows: 1) for $\vec{E}_{\text{incident}} \perp$ to plane of incidence;

$$T = \frac{2\, n \cos\theta}{n \cos\theta + \sqrt{n'^2 - n^2 \sin^2\theta}}$$

$$R = \frac{n \cos\theta - \sqrt{n'^2 - n^2 \sin^2\theta}}{n \cos\theta + \sqrt{n'^2 - n^2 \sin^2\theta}}$$

and for $\vec{E}_{\text{incident}} \parallel$ to the plane of incidence,

$$T = \frac{2\, nn' \cos\theta}{n'^2 \cos\theta + n\sqrt{n'^2 - n^2 \sin^2\theta}}$$

$$R = \frac{n'^2 \cos\theta - n\sqrt{n'^2 - n^2 \sin^2\theta}}{n'^2 \cos\theta + n\sqrt{n'^2 - n^2 \sin^2\theta}}$$

Recall that $\mu = 1$ so that $n = \sqrt{\varepsilon_r}$. For the case of normal incidence both sets of coefficients reduce to,

$$T = \frac{2n}{n' + n} \qquad R = \frac{n - n'}{n' + n}$$

Note that when n' > n R becomes negative indicating a phase reversal of the wave.

Coaxial Waveguide Modes

Since the coaxial waveguide has been chosen as the type waveguide to be used in the laboratory for propagating the pulse through model cross sections, it is necessary to know its field configurations and the frequencies of the characteristic modes. The derivation of the coaxial characteristic equation is not straight forward for the lowest order mode, the E_{oo} and since its derivation is not very common in literature it will be discussed in this chapter and included in the Appendix.

In deriving the E_{oo} mode it is interesting to note that when the wave guide boundaries are treated as perfect, there is no indication of this common mode. However, when the inner conductor is treated as an isotropic non-magnetic material of dielectric constant ε_2, which is largely imaginary, and letting Im ε_2 approach infinity, the E_{oo} mode appears without an <u>apparent</u> H_{oo} counterpart.

As shown in Figure 3 the wave guide now consists of a perfect conductor of radius a, containing a concentric inner conductor of radius b, and dielectric constant ε_2 (where ε_2 is complex).

Beginning with Maxwell's equations for a transverse wave moving in the z direction, with $\gamma^2 = \frac{\varepsilon_r \omega^2}{c^2} - k^2$ (where γ is a propagation constant);

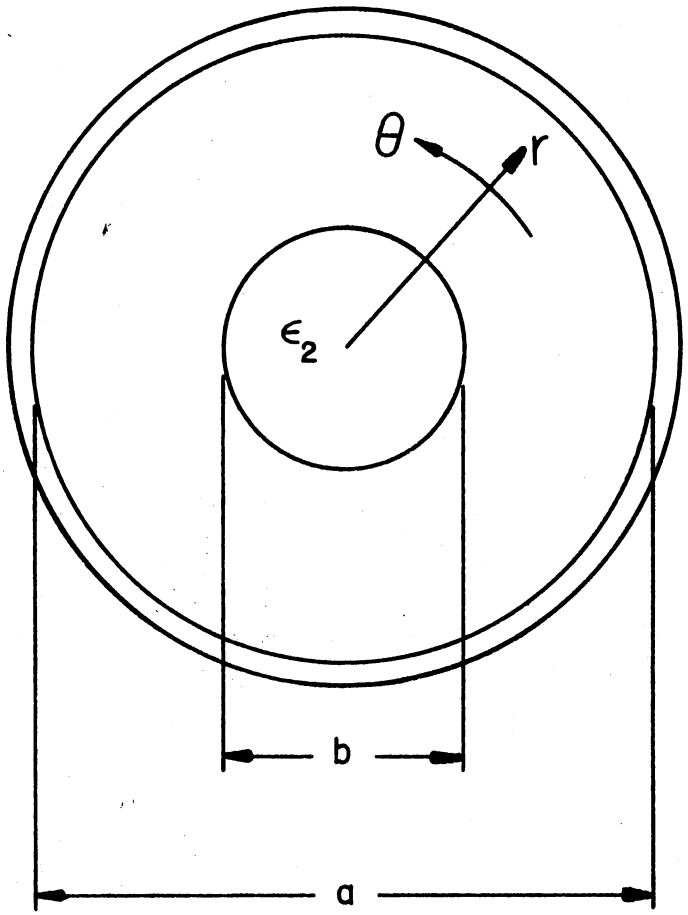

Figure 3. Coaxial Waveguide Cross Section

$$\left.\begin{aligned} \{\nabla_t^2 + \gamma_1^2\} \quad E_{z1} &= 0 \\ \{\nabla_t^2 + \gamma_1^2\} \quad B_{z1} &= 0 \end{aligned}\right\} \quad b < r < a$$

$$\left.\begin{aligned} \{\nabla_t^2 + \gamma_2,^2\} \quad E_{z2} &= 0 \\ \{\nabla_t^2 + \gamma_2,^2\} \quad B_{z2} &= 0 \end{aligned}\right\} \quad 0 < r < b$$

The solutions to these equations are Bessel and Neumann functions, which when the appropriate boundary conditions are applied to them define an eigenvalue problem (25). A characteristic equation may be derived which has a set of solutions corresponding to the permitted modes in the coaxial waveguide. The Appendix explicitly outlines the derivation of the characteristic equation beginning with the above Maxwell equations.

From Appendix the characteristic equation if for the E_{oo} mode;

$$\varepsilon_2 \gamma_1^2 = \frac{\gamma_2 J_o(\gamma_2 b)}{b J_1(\gamma_2 b) \ln(a/b)}$$

Assuming the inner conductor has an infinite conductivity, the dielectric constant ε_2 becomes almost totally imaginary;

$$\varepsilon_2 = i\varepsilon_2$$

The wave numbers for the two regions are:

$$k_1^2 = \frac{\omega^2}{c^2} - \gamma_1^2 \qquad k_2^2 = \frac{\varepsilon_2 \omega^2}{c^2} - \gamma_2^2$$

When region two is assumed to be infinitely conductive γ_2^2 becomes,

$$\gamma_2^2 = \frac{\omega^2}{c^2} i\varepsilon_2$$

The characteristic equation then becomes:

$$1 - \bar{k}^2 = \frac{(1-i)\, J_o(\gamma_2 b)}{\sqrt{2\varepsilon_2}\, (2\pi b/\lambda_o)\, J_1(\gamma_1 b)\, \ln(a/b)}$$

where

$$\bar{k}^2 = 1 - (\lambda_o{}^2/\lambda_c{}^2) .$$

When the limiting case of $\varepsilon_2 \to \infty$ is applied, the equation reduces to;

$$1 - \bar{k}^2 = 0$$

or,

$$\bar{k}^2 = 1$$

Solving for λ_c,

$$\lambda_c = \frac{\lambda_o}{1 - \bar{k}^2}$$

As $\bar{k}^2 \to 1$, $\lambda_c \to \infty$ corresponding to no cutoff frequency. In terms of k,

$$\bar{k}^2 = \frac{\lambda_o}{2\pi} k; \text{ for } \bar{k} = 1, \; k = \frac{2\pi}{\lambda_o} = \omega/c .$$

Hence, for this mode,

$$\omega/k = c = v_p$$

which defines the phase velocity to be equal to c. The group velocity is;

$$v_g = \frac{d\omega}{dk} = c ,$$

which also is c.

This derivation of the E_{oo} defines it to be a mode propagating in a waveguide with an infinite, dispositionless frequency band--identical to free space propagation.

It can be noted that the characteristic equation doesn't have a zeroth solution for the B_{oq} mode. This does not imply that the B_{oo} mode doesn't exist. From the field equations in Appendix I, the various components of the $\vec{E}$ and $\vec{H}$ fields are;

$$E_z = E_o = B_z = B_r = o$$

$$E_r = q_i/(2\pi\ re)$$

$$B_\theta = q_i\omega/(\gamma 2\pi r)$$

This defines the field configurations in the waveguide; a cross-sectional plot is shown in Figure 5. The only non-zero components are the radical electric and ozmuthial magnetic fields. Both which are transverse to the waveguide axis, constituting a TEM wave. This is expected since $\lambda_c = \lambda$, as common to all TEM waves.

Although the B_{oo} cannot be explicitly derived, inductive reasoning reveals that the E_{oo} and B_{oo} modes must be one and the same. They are indistinguishable and both propagate at a group and phase velocity, c. This is fortunate in that only one dispersionless mode exists in an infinitely wide operating band. Using the impulse described in the next section, the E_{oo} will be the only mode excited in the waveguide, however, if there were any other modes near to the E_{oo}, using such a wideband impulse would surely excite them also and since they may have a different phase velocity the pulse shape may become distorted after traveling any length of the waveguide. Figure 4 shows the frequency location of the higher order modes as a function of the ratio of a/b,

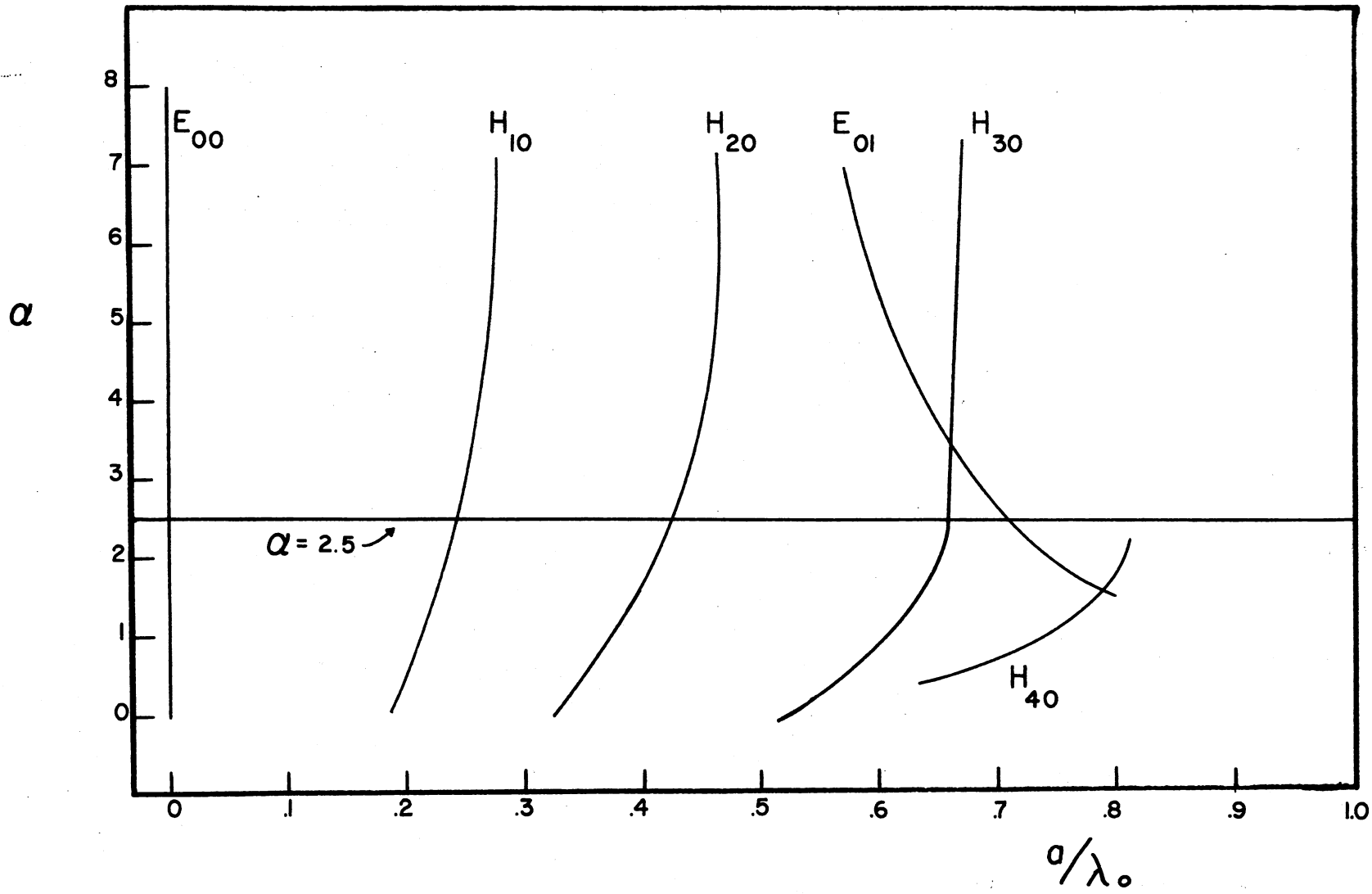

Figure 4. Cutoff Frequencies of Common Coaxial Waveguide Modes

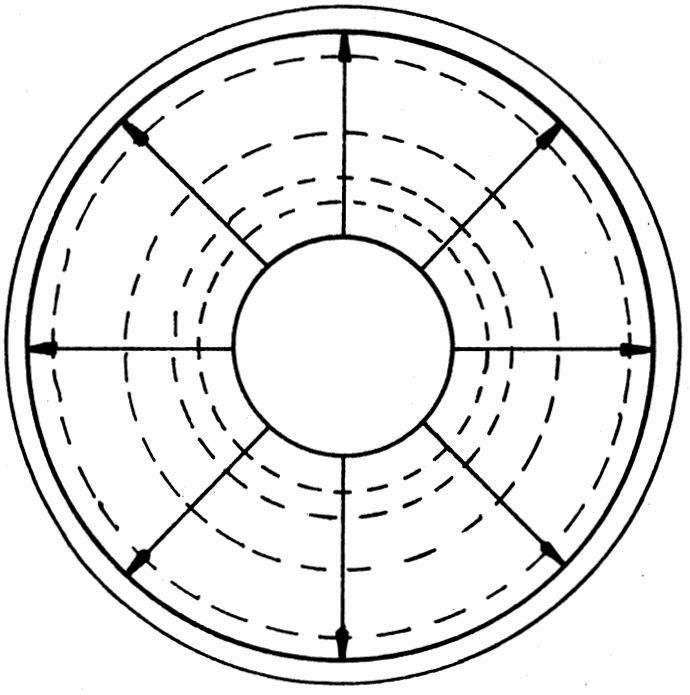

Electric Force Lines

Magnetic Force Lines

Figure 5. Field Configuration in Coaxial Waveguide

for the waveguide constructed for this experiment the next mode to appear is the H_{∞} at 3.0 Ghz, well above the pulse's frequency band.

Also from Figure 5 the field configuration of the E_{oo} mode is shown and can be seen to always be transverse to the direction of propagation and directed radially from the axis. Therefore any interface that is perpendicular to the waveguide axis will have its plane of incidence normal to the E_{oo} wave, thus the reflection and transmission coefficients reduce to their simplest form.

Characterization of the Impulse

The ultrashort impulse required for time resolution by the reflectometer was produced by a pair of sparkgaps contained in a coaxial waveguide section, the mechanisms of which will be thoroughly discussed in Chapter III. This section will be only concerned with the mathematical characterization of the impulse in the time and frequency domain.

The impulse generated by the sparkgaps was a relatively large voltage impulse with a magnitude of 8.5 KV, and a one nanosecond duration (1/2 power width). This corresponds to a peak power of 1.44×10^6 watts delivered to a 50Ω load. For a 1 KHz repetition rate the average power is only 1.44 watts. The pulse shape, in particular the leading edge was considered to be the most critical parameter of the pulse once the short duration was obtained. This is due to the fact the leading edge has the steepest slope, approximately 200 picoseconds, thus is the largest contributor to the frequency components. Any large amount of jitter would cause the frequency components to vary. This could possibly lead to pulse distortion, decreased time resolution, and the production of an apparent dispersion effect. Eventually the source was modified so as to

produce a stable risetime with only a few percent of jitter enabling a determination of the operating frequency region.

In order to obtain the frequency spectrum of the impulse by means of a fourier transform, the pulse had to be explicitly defined. From Figure 6, the pulse shape appears to be a non-symmetrical gaussian shaped curve since the leading edge is a steeper exponential than the trailing edge. However, to make the transform practical by other than numerical methods, a single smooth function should be found that describes the entire impulse. Even if a function only approximate s the impulse it should be satisfactory since only the approximate frequency spectrum needs to be known.

A function that nicely approximates the impulse was found to be the Gamma Distribution function;

$$f(t) = \text{constant} \frac{(\alpha t)^{x-1} e^{-t\alpha}}{\Gamma(x)}$$

where x is a constant which must be empirically chosen (1). A choice of $x = 1.5$ where $\Gamma(x) = \sqrt{\pi}/2$ and $\alpha = .5 \times 10^{-9}$ sec^{-1} was found to produce the impulse shaped distribution. Letting the constant be 8.5 KV, the distribution is plotted in Figure 7 with the impulse. It can be seen that the resemblance is strongest at the leading edge and less on the trailing edge, hence the most important contributions from the steep risetime are preserved.

The fourier transform of the gamma distribution function to the frequency domain is;

$$F(\omega) = \frac{\text{constant}}{\alpha\left(1 - \frac{i\omega}{\alpha}\right)^{x}}$$

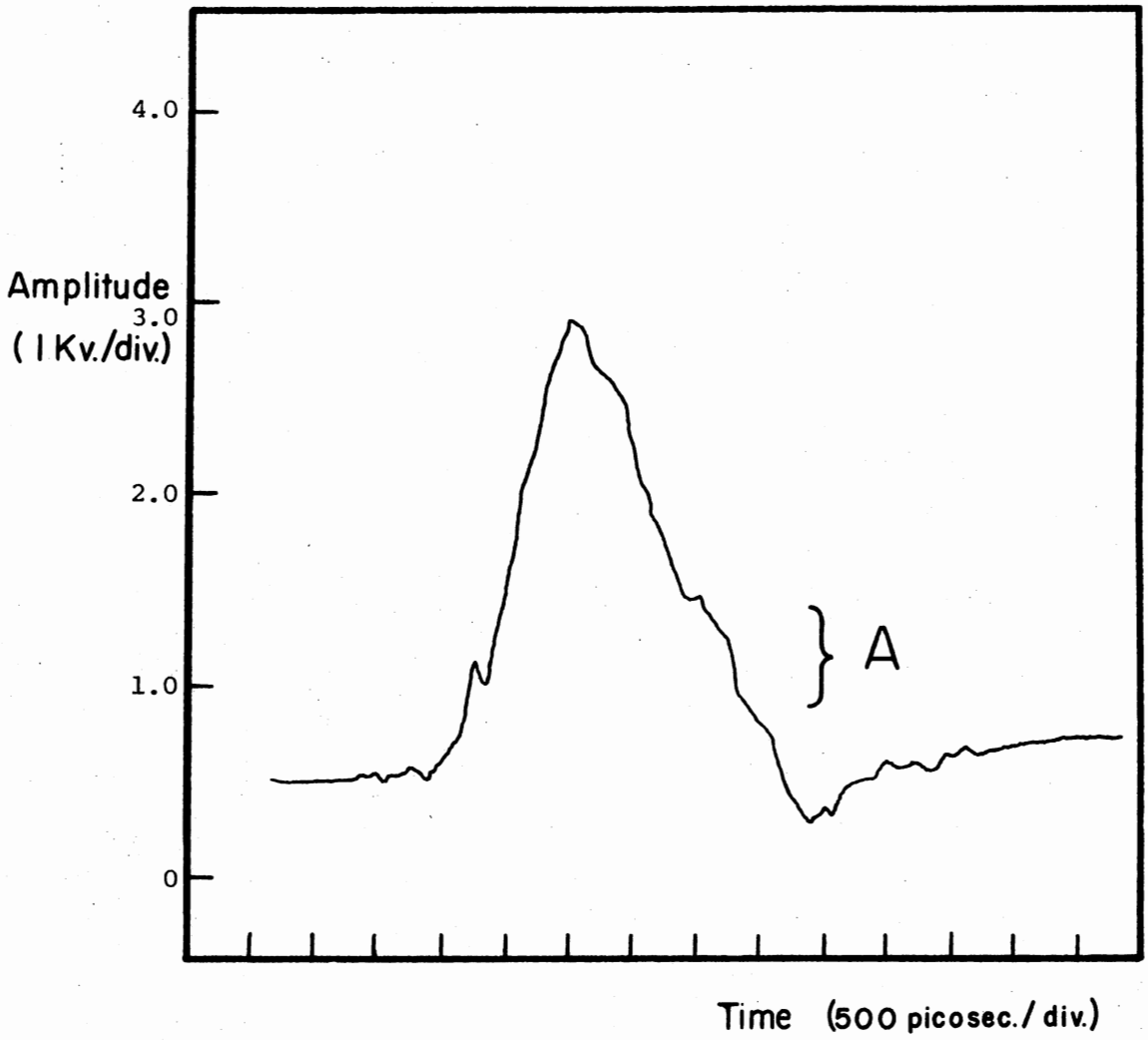

Figure 6. Oscilloscope Trace of the Impulse

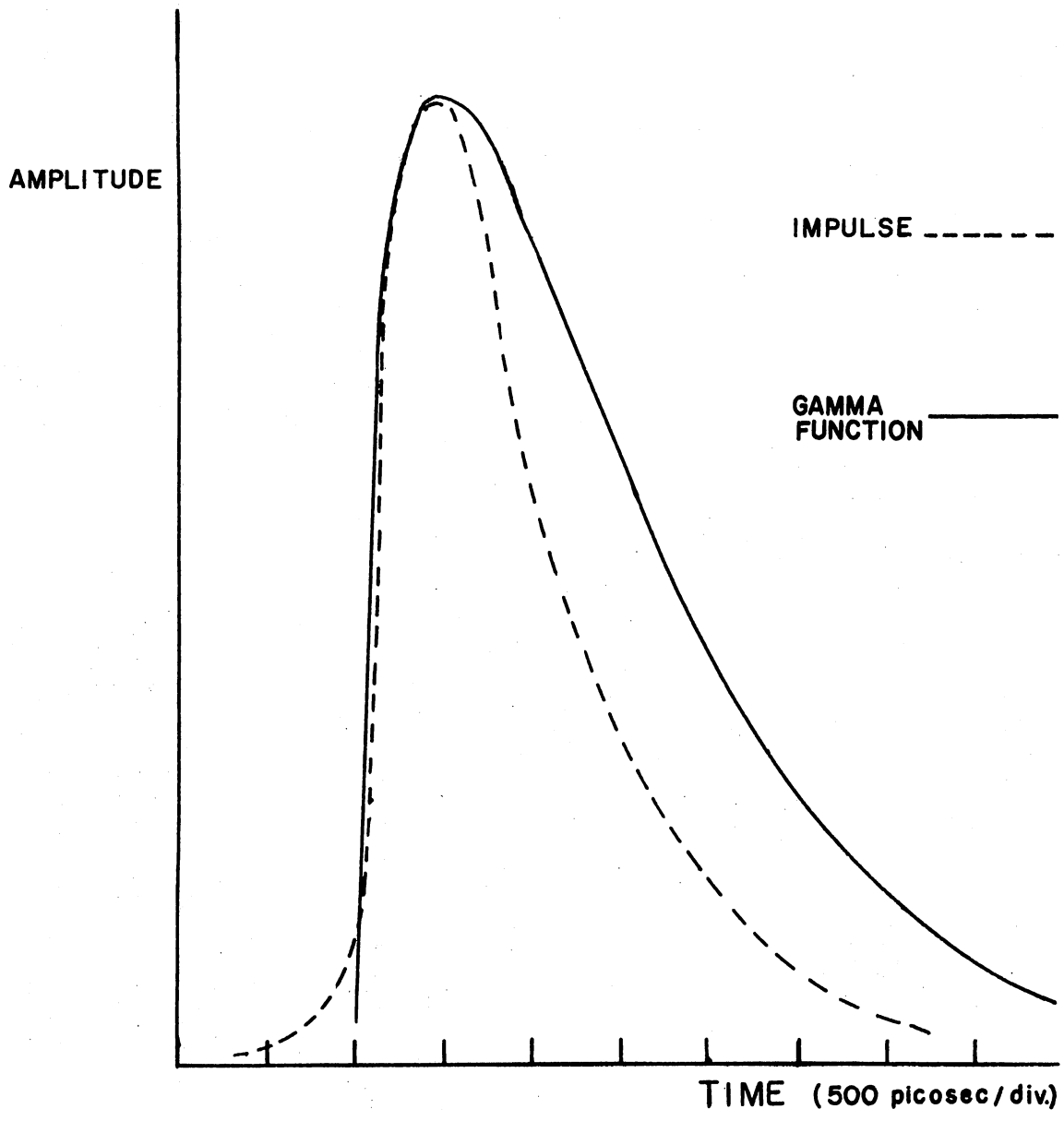

Figure 7. Gamma Distribution Function Approximating Impulse

This transform results in the frequency dependent function being complex (21). The imaginary portion contains phase information of the various frequency components. The absolute value of the transform will describe the frequency spectrum, however it will be at a loss of this phase information. The absolute value of frequency transform is;

$$|F(w)|^{\frac{1}{2}} = \frac{\text{constant}}{\alpha\left[1 + \left(\frac{\omega}{\alpha}\right)^2\right]^{x/2}}$$

The absolute value gives information concerning the magnitude of the various frequency components, as shown in Figure 8. As can be seen in the figure, the components all have about the same magnitude over a very broad band (0 to 10^6 hz). Around the several hundred megahertz region the magnitude begins to roll off and even up to 5 Ghz the impulse contains significant components.

Reflectivities

Recalling the transmission and reflection coefficients, T and R respectively, for the E_{oo} mode hence normal incidence, an expression for the detected amplitude of a reflection from the ith interface in a layered complexion may be derived.

Constructing a model of the layered systems, as shown in Figure 9, it consists of i = 1,2,3,...j different layers each possessing an index of refraction n_1, n_2,...n_j (where $n_i = \sqrt{\varepsilon_i}$) and a thickness x_i. Specifying that the impulse source and the detector are both in the first layer, any discontinuity between the generator and or detector may be taken into account as the first interface.

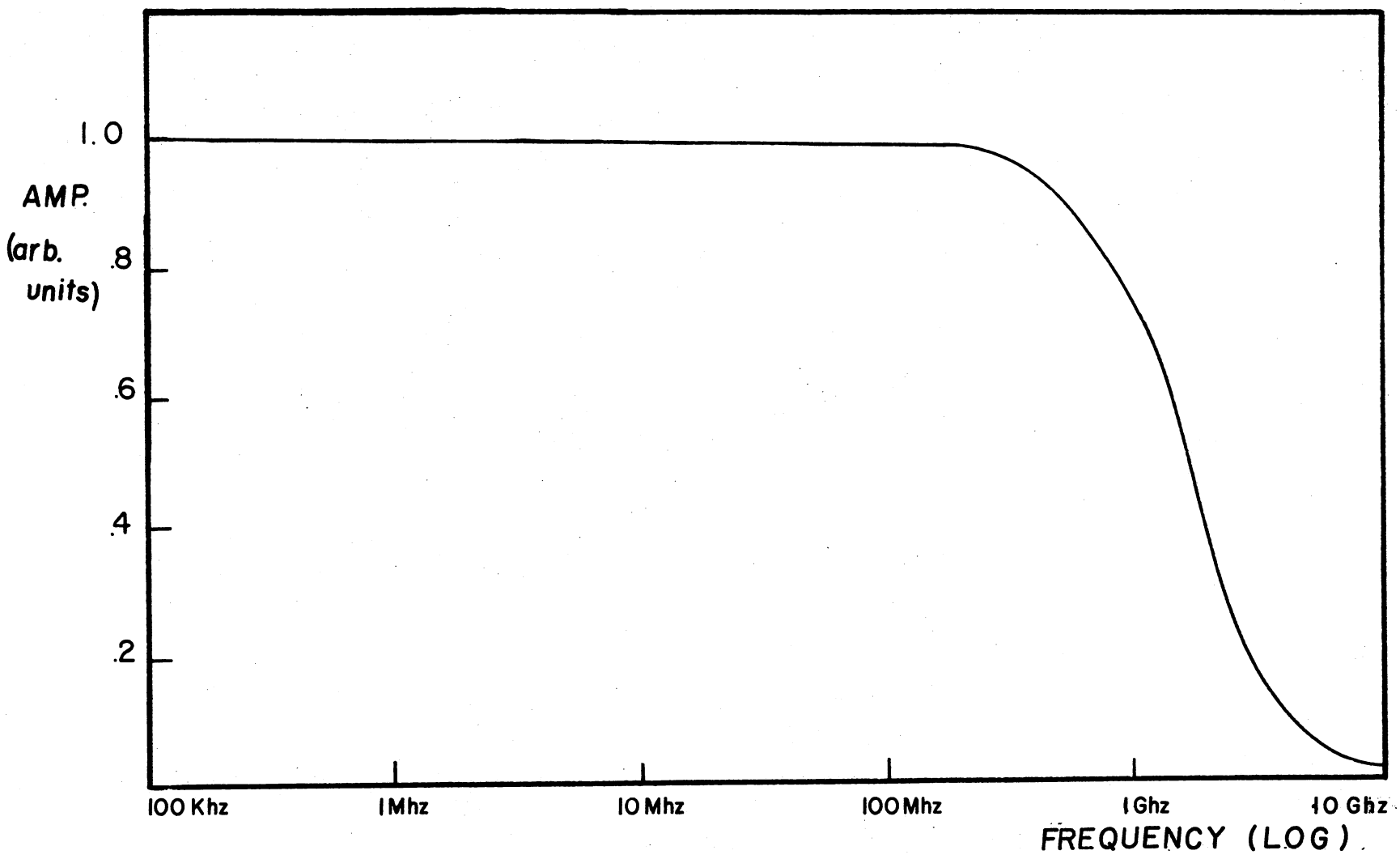

Figure 8. Fourier Transform of the Impulse

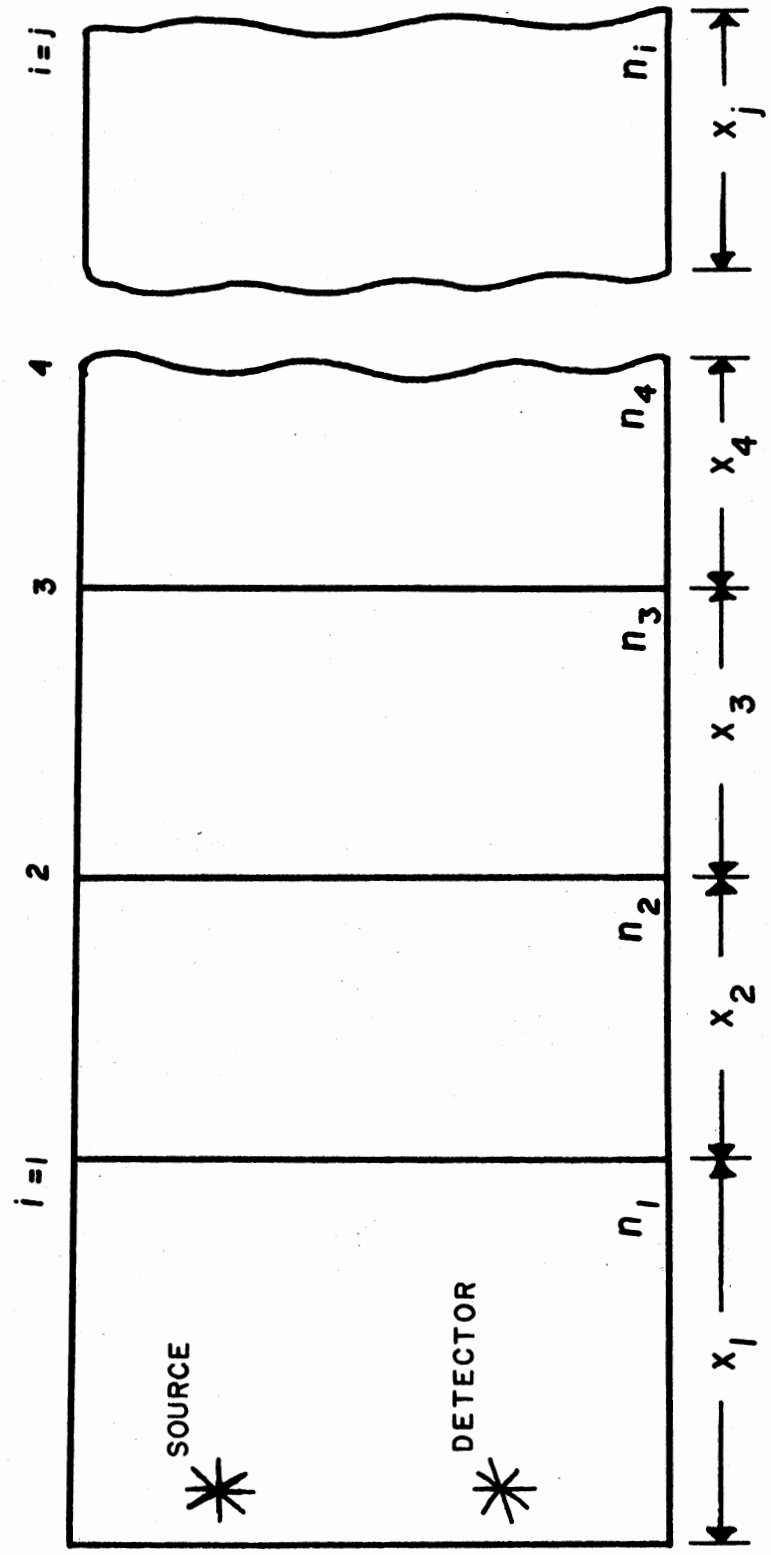

Figure 9. Layered Medium Model

Denoting the impulse amplitude to be A_o in region 1 and the amplitude detected of a reflection from the interface between layers i and i+1 to be A_1, such that,

$A_1 = A_o R_{12}$ is the first reflection, and

$A_2 = A_o (T_{12})^2 R_{23}$, since $T_{12} = T_{21}$, is the second, and

$A_3 = A_o (T_{12})^2 (R_{23})^2 R_{34}$ is the third and so forth.

Now, substituting the expressions for T and R a reflection from the fifth interface would appear as:

$$A_5 = A_o \left(\frac{2n_1}{n_1 + n_2}\right)^2 \left(\frac{2n_2}{n_2 + n_3}\right)^2 \left(\frac{2n_3}{n_3 + n_4}\right)^2 \left(\frac{2n_4}{n_4 + n_5}\right)^2 \left(\frac{n_6 - n_5}{(n_5 + n_6)}\right)$$

Thus in general a reflection from the ith interface would have a detected amplitude of;

$$A_i = A_o \, 4^{i-1} \left[\prod_{\substack{j=2 \\ \text{for} \\ i>1}}^{j=i} \left(\frac{n_j - 1}{n_{j-1} + n_j}\right)^2\right] \left(\frac{n_{i+1} - n_i}{n_i + n_{i+1}}\right)$$

This expression may be modified to include any attenuation if it is present, as long as the attenuation coefficients are known. Since the amplitude is attenuated by a factor or $e^{-\alpha x}$, a two way passage through layer k will be decreased by $e^{-2\alpha x}$. Thus a reflection from interface i will have a detected amplitude of:

$$A_1 = A_o \, 4^{i-1} \left[\prod_{\substack{j=2 \\ \text{for } i>1}}^{j=i} \left(\frac{n_j - 1}{n_{j-1} + n_j}\right)^2\right] \left(\frac{n_{i+1} - n_i}{n_i + N_{i+1}}\right) \cdot \exp \sum_{\ell=1}^{\ell=i} \alpha_\ell 2x_\ell$$

so that if there is no attenuation present the last term becomes unity.

Time of Flight

The above expressions only predict the detected amplitudes for layers of various dielectric constants without respect to the reflection's position in time. However, the reflected pulses time position with respect to the incident pulse may be determined from the layer thicknesses and the dielectric constants (velocity). The time it takes for the pulse to travel to interface i and be reflected back to the detector is:

$$t = 2\left\{\frac{x_1}{v_1} + \frac{x_2}{v_2} + \frac{x_3}{v_3} \cdots\cdots \frac{x_i}{v_i}\right\}$$

and since the velocity v i is $c/\sqrt{\varepsilon_i}$ the time becomes:

$$t = \frac{2}{c}\{x_1 n_1 + x_2 n_2 \cdots\cdots x_i n_i\}$$

or if the time difference between two consecutive reflections from interface i and i+1, is Δt, then the dielectric constant of layer i is;

$$\varepsilon_i = \left(\frac{2x_i}{c\Delta t}\right)^2 \quad \text{or;} \quad n_i = \left(\frac{2x_i}{c\Delta t}\right)$$

thus the dielectric constants may be determined from two separate mechanisms.

CHAPTER III

IMPULSE SOURCE

Description of Design

One of the fundamental problems in developing a time domain reflectometer was the generation of the ultrashort impulse at a power level such that reflections from a multilayered medium could be detected, even in the presence of moderate attenuation. It was estimated that a multikilovolt pulse with a duration of the order of 1 nanosecond was required. Since a source of this description was not commercially available it was decided to design and construct one similar to a device concepted by D. F. McDonald and C. J. Benning of the University of Texas. Their design consisted of a coaxial cylinder containing two spark gaps externally connected to a capacitor discharge circuit as shown in Figure 10 (19).

The construction of the source proved to be one of the more difficult and time consuming portions of building the reflectometer. The original device constructed from aforementioned concept had some basic problems and it was not until several modifications had been made that it provided a satisfactory impulse. This chapter details the design and construction of the generator along with the theory of how it produces the impulse.

The first generator constructed was similar to McDonald's and Benning's device except that the pressurized second gap was replaced

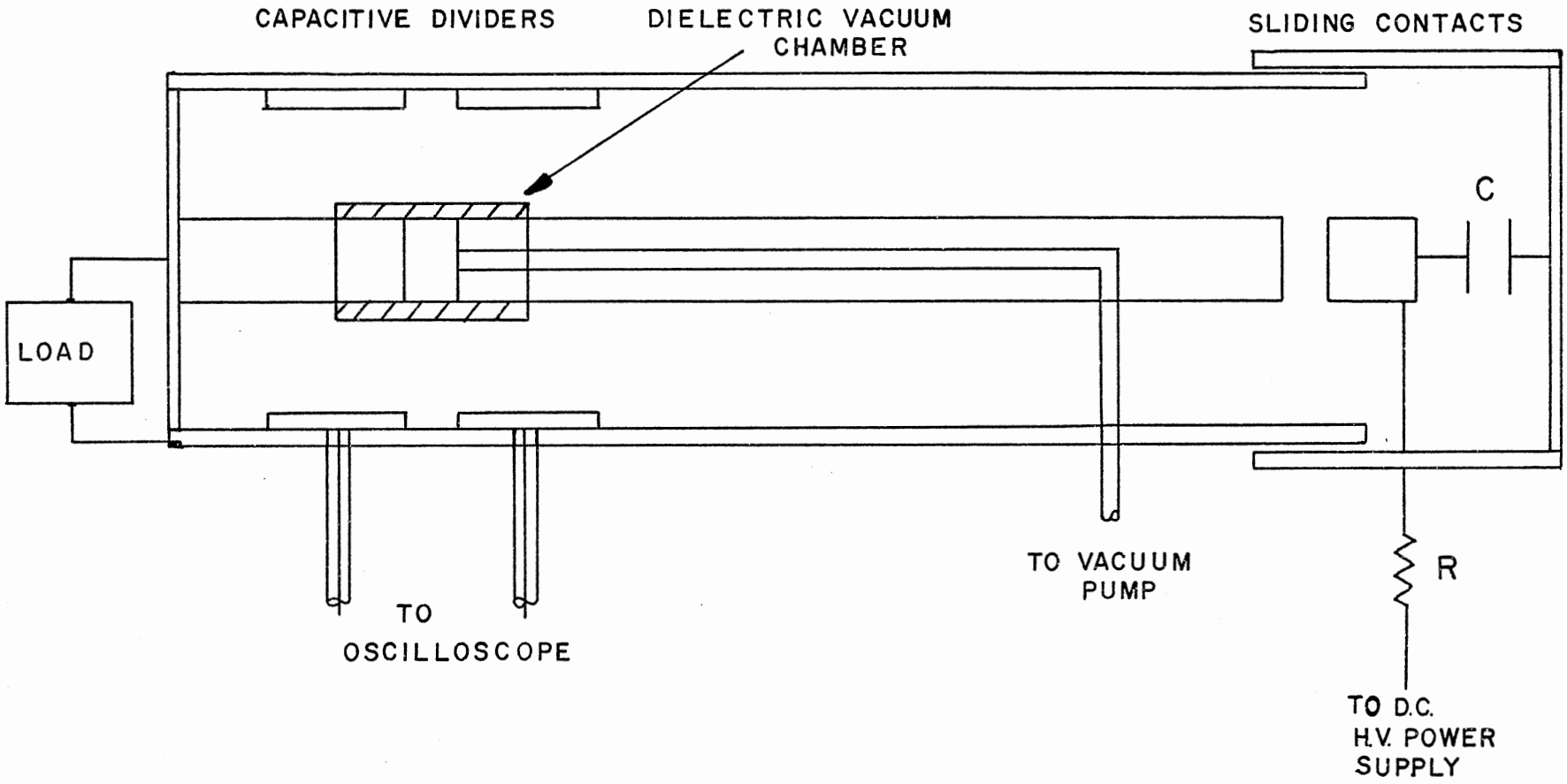

Figure 10. McDonald and Benning Gas Discharge Impulse Generator

with an atmospheric one. This was done in order to facilitate construction and minimize any discontinuities in the coaxial cylinder (22). Also, a constant impedance (50 ohm) adapter was attached in order to electrically connect the load to the generator since the impulse will contain microwave and U.H.F. components.

Other modifications included changing the coaxial cylinder's impedance to 50 ohms, externally positioning the charging capacitor and shortening the inner conductor. Since the inner conductor determines the pulse length, as will be discussed shortly, the length was made so as to produce a one nanosecond pulse whereas McDonald and Benning had a long inner conductor so as to produce step type impulses.

The first generator constructed, along with its power supply, is shown in Figure 11a. The gaps were both externally adjustable and the cylinder constructed to withstand slight overpressures and fair vacuums. However, under a variety of gap settings, gases and pressures, the generator would only produce pulses with widths being on the order microseconds. A closer examination of these pulses revealed the presence of thousands of smaller pulses forming the large pulse as shown in Figure 11b. The problem was found to be caused by the discontinuity between the cylinder and the power supply cable; when the external capacitor was discharged, part of the power was reflected back to the power supply where it was again reflected back to the tube causing it to pulse again. This continued until the capacitor was fully discharged. The problem was remedied by making the line from the power supply to the first gap a constant impedance (50 ohm) path and also by making the cable long enough so that any reflections caused by the spark gap would not be reflected for a few hundred nanoseconds, thus would not interfere with

a.

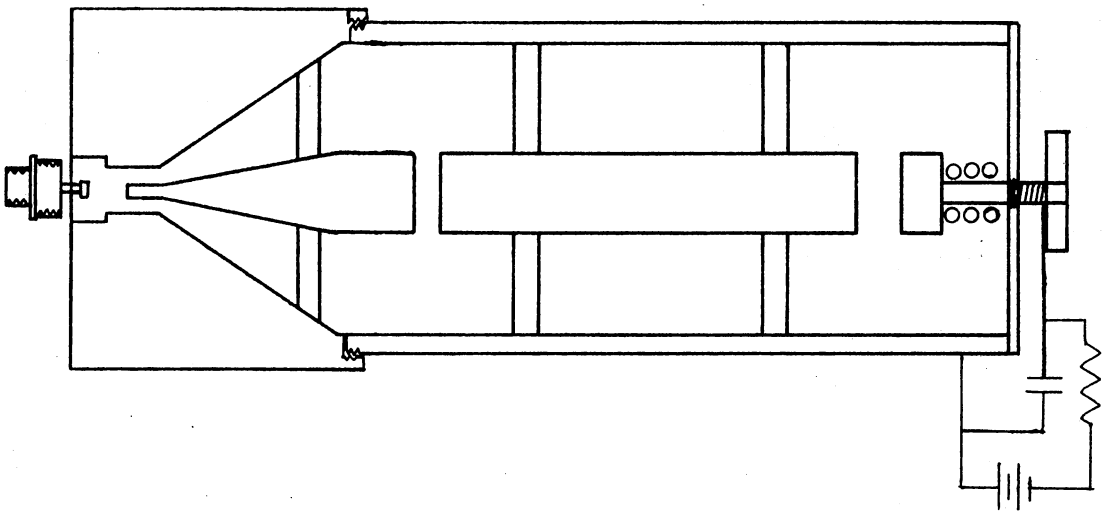

b.

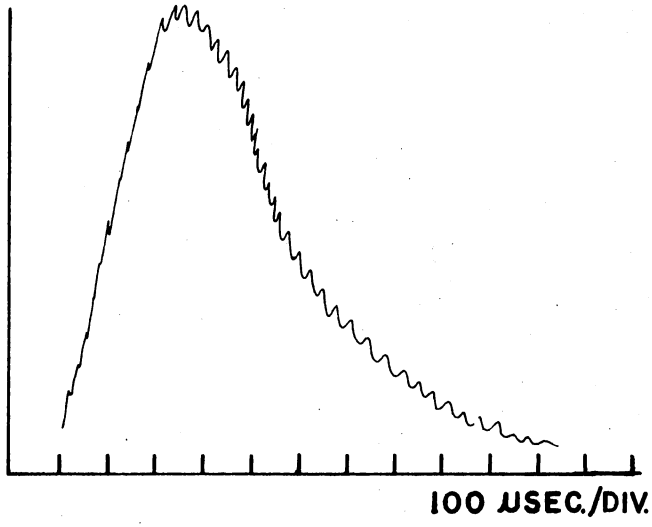

Figure 11. (a) First Impulse Generator Design; (b) Impulse This Generator Produced

any measurements.

Figure 12 shows the final configuration that was successful in producing a high voltage nanosecond impulse.

Theory of Operation

Before the mechanisms of the impulse production can be discussed, the most important aspects of the generator should first be looked at, that is, the electrical breakdown between two electrodes, as occurs in the spark gaps.

Analysis of Electrical Discharges

The fundamental process of an electrical discharge refers to the passage of a current through a gaseous medium which is characterized by ionization. Various terms have been given to the discharges depending upon the amount of current the breakdown allows to flow. For the impulse generator, these currents are in excess of .1 amps thus are termed transient arc discharges (5).

At standard conditions, any gas may be assumed to contain a certain percentage of ionized particles and free electrons. In the absence of an electric field there exists an equilibrium such that the rate of ionization balances the rate of recombination. Now consider placing two planar electrodes, such as is in the coaxial cylinder, and by placing a potential between them, creating an electric field. For very small field strengths, there exists a very small current flow due to the movement of charged particles existing in the gas. This is known as a Townsend discharge (3). The current continues to increase as the field increases until the field begins to sweep out more charged particles

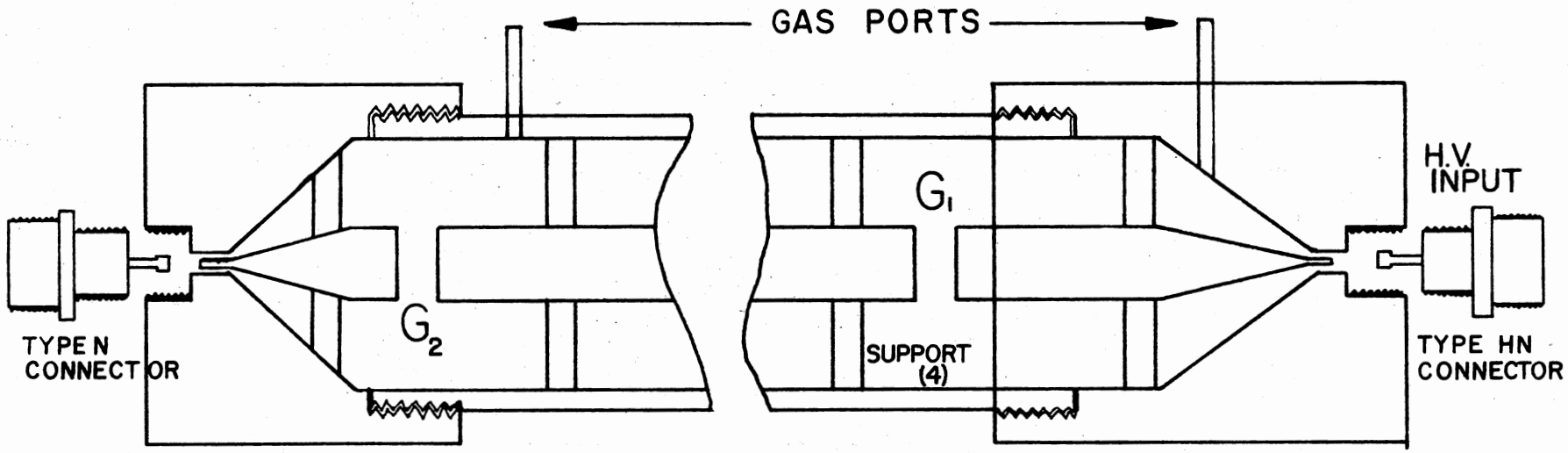

Figure 12. Gas Discharge Device Capable of Producing One Nanosecond High Power Impulses

than the other mechanisms, whatever they may be, produce. The current then no longer increases with increasing electric field strength, as seen in Figure 13. However, as the field strength becomes even larger, there exists a point where the current exponentially avalanches to the maximum value the components external to the electrode will supply, known as a breakdown. The value of the potential, where the increase of current continues with no further increase in field strength, is known as the static breakdown potential, V_B. The reason the avalanche occurs, even in a gas that contains few charged particles, is that the electric field is intense enough to accelerate a single electron so that when it collides with a neutral gas atom it has enough energy to ionize it. This results in a chain reaction type ionization process, sometimes known as an electron avalanche. This process usually occurs so rapidly that the more massive ions remain relatively stationary. As shown in Figure 14, the number of electrons rise with position and time analogous to an avalanche. The space charge of electrons must not become so dense so as to distort the electric field greatly (6). This mandates the use of electrodes that have a large diameter with respect to the gap spacing.

Looking at the gap as shown in Figure 14, consider a charge q initially located near the cathode and due to the electric field, creates an avalanche. Assuming the ions remain at rest, in a field strength E, the charge grows according to

$$q(x) = e \cdot n_o e^{\alpha x} .$$

n_o is the number of electrons per second appearing at the cathode, thus, $e \cdot n_o = q_o$, and α is the Townsend first ionization coefficient determined by the gas, pressure, and electric field strength. Since,

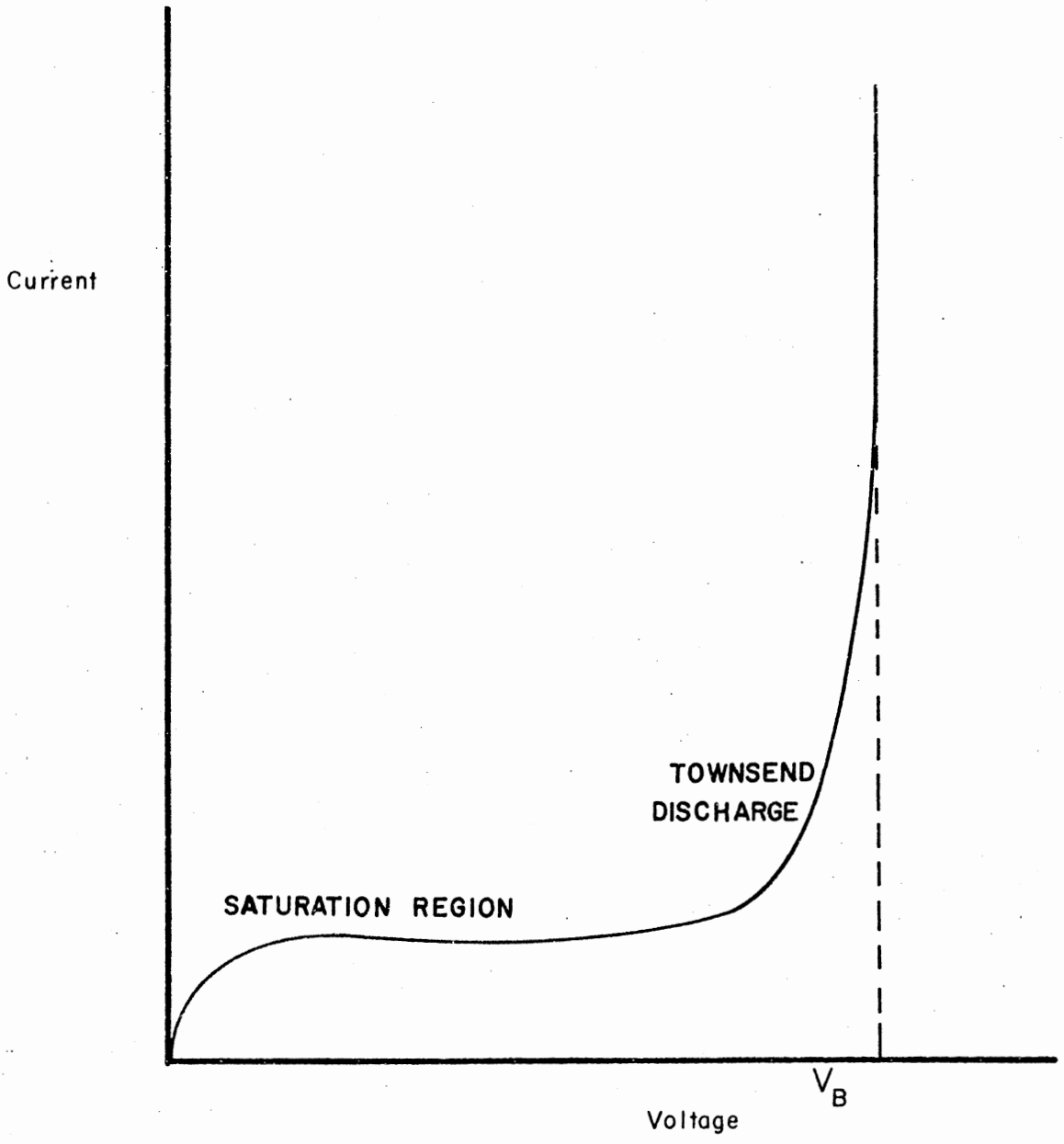

Figure 13. Discharge Characteristics in Townsend Region

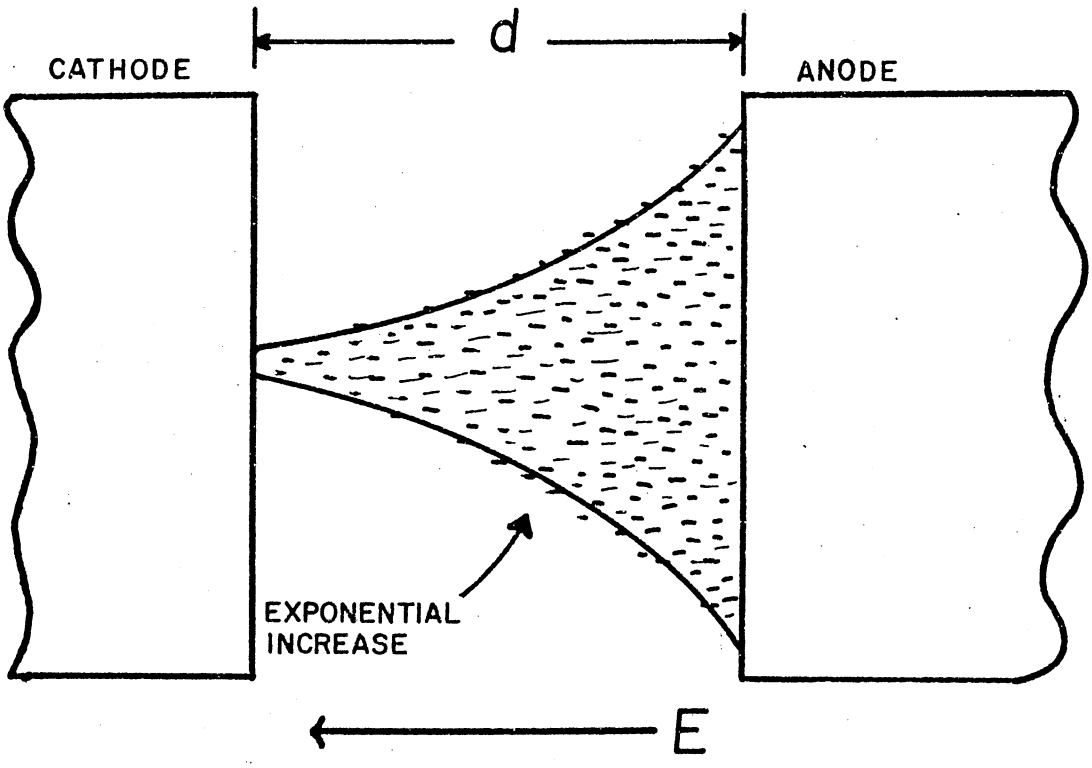

Figure 14. Electron Avalanche Between Two Planar Electrodes

$$iVdt = q(x)\,Edx, \text{ and } dx/dt = v$$

the current, i, at any instant, may be expressed as:

$$i(t) = q_o \frac{v}{d} e^{\alpha v t} = q_o \frac{v}{d} e^{t/\tau}$$

where d is the gap width, and τ is the exponential time constant:

$$\tau = 1/v\alpha$$

The time constant τ should approximate the risetime of the impulse (9).

In a molecular gas v_- is the drift velocity of the electrons and is determined by the electric field strength, the pressure, and the mean free path (13). The drift velocity is defined as the velocity due to the average kinetic energy of an electron after numerous collisions. An analogy is the terminal velocity obtained by a body in a vicous media under the influence of a constant force.

Defining the drift velocity of electrons, v_-, as;

$$v_- = k\,E$$

Where the proportionality constant, k, is known as the mobility and is determined by the gas and the pressure.

Defining the average kinetic energy of an electron in an electric field as $eE\lambda_e$, where e is the electronic charge and λ_e is its mean free path, so that:

$$E = eE\lambda_e = \tfrac{1}{2}mv_-^2$$

and expressing the mean free path as,

$$\lambda_e = \frac{1}{\sqrt{2}\,\pi\,nd}$$

where n is the molecular density and d an atomic diameter (13).

The generator was found to operate best when the gas argon was used, with the second gap set at 9 mils (.023 cm). Estimating an electrode potential of 3 KV, the electric field produced between the electrode is 1.3×10^7 V/m. Thus the average drift velocity is roughly,

$$v_- = 8.5 \times 10^5 \text{ cm/sec}$$

From Figure 15 the coefficient α may be determined for argon; for

$$E/P = 172 \frac{V}{cm} \cdot \text{mmHg}, \quad \alpha/P = \frac{4 \text{ ion pairs}}{cm \cdot \text{mmHg}}$$

therefore, α = 3040 ion pairs/cm, (1). The time constant, τ, may now be calculated,

$$\tau = 1/v_-\alpha = 3.9 \times 10^{-10} \text{ seconds} = 390 \text{ picoseconds} .$$

As can be seen in Figure 6, this corresponds very closely to the impulse risetime.

Now that steady state breakdown process has been discussed, the breakdown that occurs when the gap is pulsed with a potential $V \geq V_B$ can now be looked at (6). The critical factor is, in this case, that first electron that appears at the cathode and initiates an avalanche. It is not likely that every electron that appears at the cathode may lead to an avalanche, but the one that does is termed the primary one.

Once the gap is pulsed with an overvoltage, the time required for breakdown can be divided into the statistical and formative time logs. The statistical time lag is the interval between the application of the overvoltage and the appearance of the primary electron. The formative time lag is the time required for the breakdown to maximize once

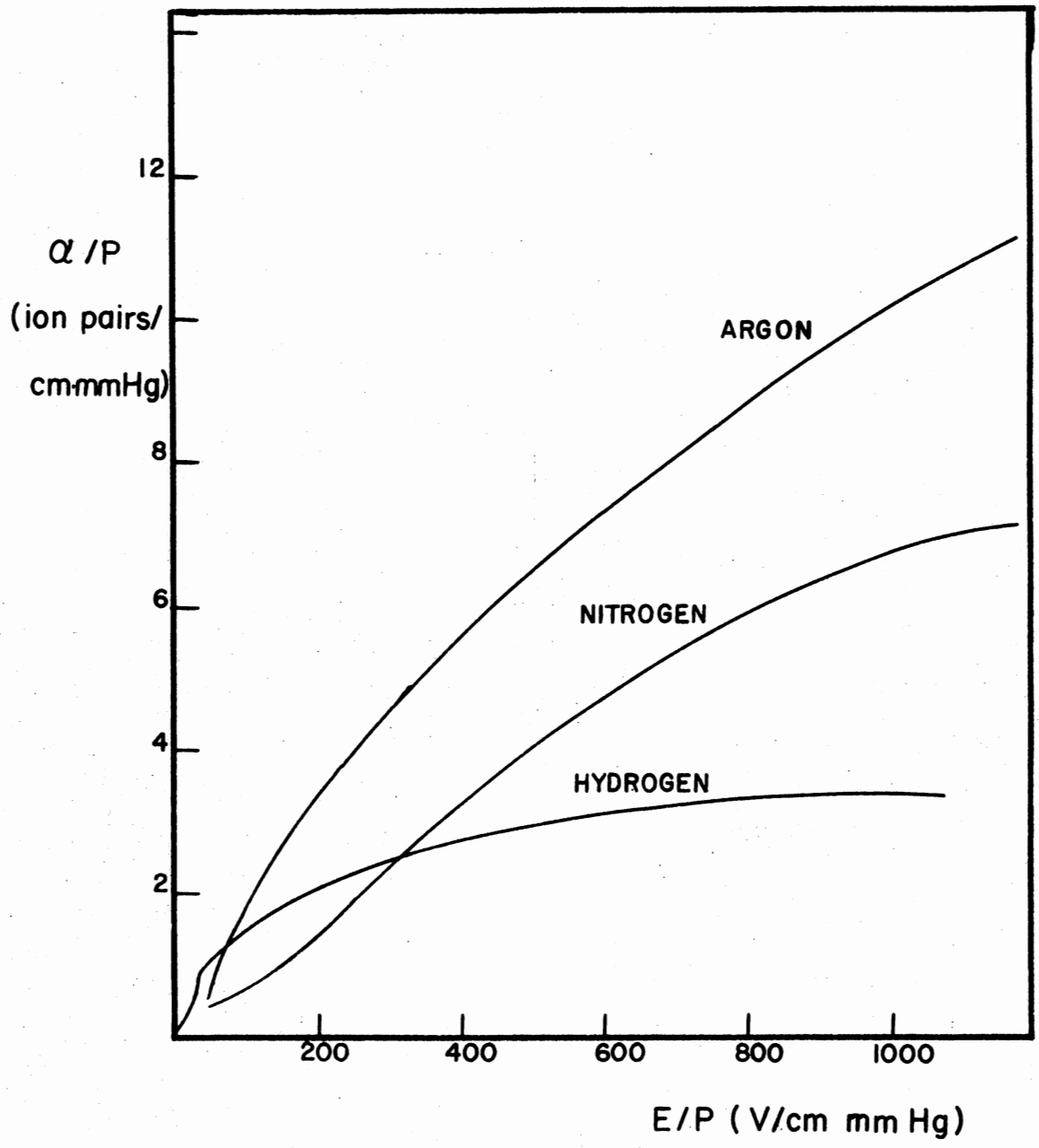

Figure 15. 1st Townsend Ionization Coefficient as a Function of E/P

initiated (this is the time constant previously calculated (3).

The statistical time lag is controlled primarily by the electron density of the gas and the electric field strength. The electron density may be externally controlled by ionizing the gas. For the generator constructed, the aluminum electrodes had fairly high electrom emission rates (about 10^4 electrons/sec) thus no external gas ionization was required. The higher the overvoltage, $V-V_B$, the larger the probability that an electron appearing at the cathode would become a primary electron thus initiating a breakdown. Once the breakdown occurs, it is selfsustaining as long as the external components supply charge.

Mechanisms of the Impulse Formation

Now that the breakdown in the gaps has been detailed, the method that the coaxial discharge tube produces the impulse can be described.

Various gases, pressures, and gap spacings were used in the cylinder. The most critical parameter appeared to be the type of gas used. Argon, air, helium, and nitrogen were all used as environments for the discharges, with argon being superior to the others in producing a subnanosecond risetime, stable repetition rate, and least amount of jitter. Nitrogen worked well for short operating periods, but due to the long lived oxides of nitrogen that were produced, the environment soon became contaminated and operation erratic. Helium and air caused very erratic operation.

Using argon, the first gap spaced at 18 mils (.046 cm) and the second at 9 mils (.023 cm) resulted in the best impulse. A slight argon flow was used instead of a static pressure; it is not known exactly why the flow is better, but it does produce a stable repetition

rate. Perhaps due to a more uniform statistical time lag since the gap is more quickly replenished with electrons.

A schematic of the external power supply and the coaxial discharge tube is shown in Figure 16. Initially starting with all capacitances discharged, the formation of an impulse will be described.

The power supply usually supplied about 4.5 KV to the R-C circuit which had a time constant of .001 second, and determined the tube's repetition rate. Denoting the static breakdown potential of the first gap V_{B1}, the first gap broke down shortly after the external capacitor had surpassed a potential of V_{B1}. When this occurred, the capacitance associated with the inner conductor began to store charge. The capacitance of the center section is 16.8 picofarads, thus the external capacitance had only to lose 1/2000 of its total charge in order to create a zero potential across the first gap.

An unknown factor in this charging of the center section is; at which potential (across the gap) does the discharge self extinguish. Estimating from the ratio of the width of the second gap to the width of the first, it appears that the discharge ceases when the inner rod has stored enough charge so the potential across the first gap is about $1/3\ V_{B1}$.

Now that the inner section is charged, a potential appears across the second gap, which is approximately 2.5 - 3.0 KV. This potential is approximately 100% greater than V_{B2} thus the statistical time lag is very short, probably on the order of microseconds, before breakdown occurs.

When the second gap breaks down, it does so with a formative time (approximate risetime) of roughly .390 nanoseconds. However, since the

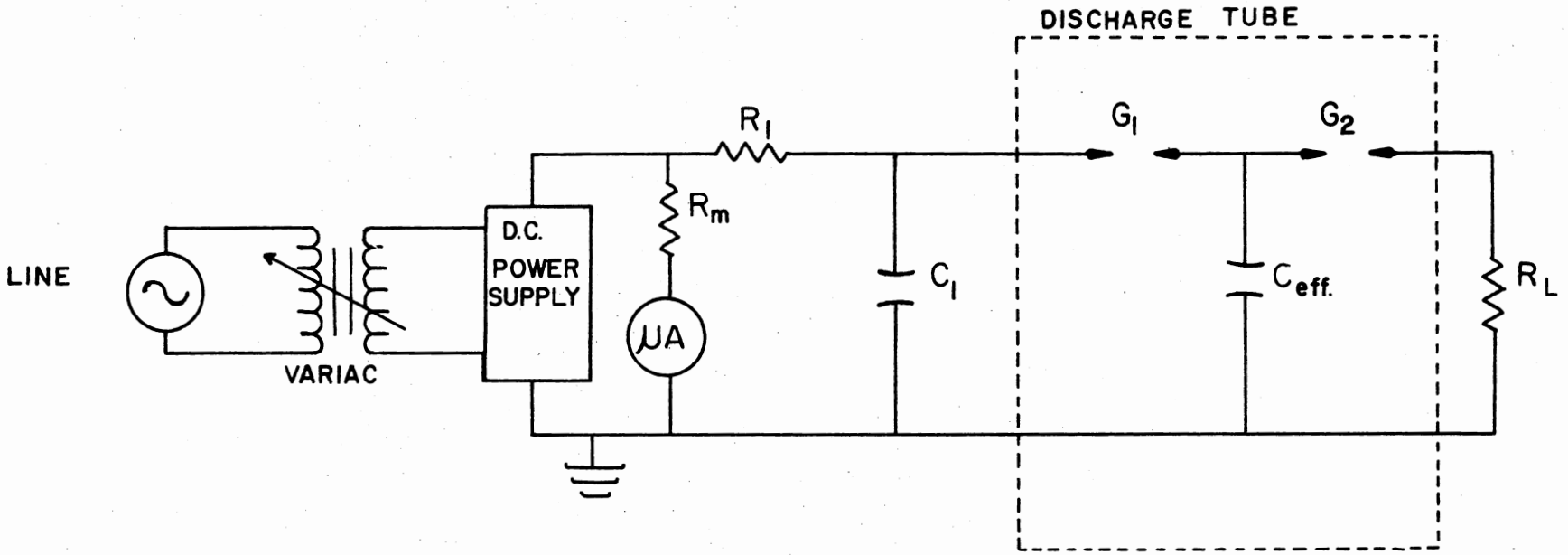

Figure 16. Schematic Representation of Discharge Tube and Power Supply

capacitance of the load and attached cable is much greater than the inner section, the discharge will be rapid. The risetime is determined by the electron avalanche and the falltime is determined by the discharge characteristics of the inner capacitance. As shown in Figure b, the trailing edge appears as a normal capacitor discharge until a particular point A, that point is about 1/3 V_{B2} and is where the discharge ceases, probably in an antiavalanche manner as can be seen by the curve suddenly broadening.

CHAPTER IV

THE REFLECTOMETER

Waveguide

In order to be able to practically and accurately investigate the electrical properties of layered terrestrial materials, it was decided to use waveguides that could be filled with the samples and set up in the laboratory. Given the source described in Chapter III and from its frequency spectrum in Chapter II, it may be seen that the center frequency is too low and the width too wide for most of the common waveguides (20). However, the coaxial waveguide possesses a "transmission line mode" (E_{oo}), that has an infinite cutoff wavelength, this mode, along with others common to the coaxial waveguide, has been explicitly derived in Chapter II. Thus with an infinite bandwidth, this type of guide would not have any dispersion which may distort the impulse. Also, since the only critical dimensions are the inner and outer diameter ratio, d, the guide may be constructed of a practical size.

When choosing α, the primary consideration was to preserve the 50 ohm impedance of the system. Next in mind was to facilitate the waveguide construction by using standard size rod and pipe. A compromise of $\alpha = 2.5$ was finally used. This produced a waveguide impedance of:

$$Z = 60 \ln \alpha = 54.9 \text{ ohms} .$$

For a choice of $\alpha = 2.5$, the modes may be located with respect to

frequency, see Figure 4. The closest mode to the E_{oo} is the H_{01} which begins to appear at 3.0 Ghz. Since this mode will have a smaller velocity close to its cutoff frequency, any excitation of this mode may result in the impulse being distorted. However, from Figure 8, it can be seen that there are few, if any, frequency components that would contribute to the excitation of this mode.

The physical construction consisted of sections 1.20 meters in length, and made in such a way that each section may be joined together. This is shown in Figures 17 and 18. By filling the sections with various liquid and solid dielectric samples, a stratified system may easily be compiled. As seen in the diagram, each section has two plexiglass seals at opposite ends. These may appear as discontinuities to a propagating pulse, however, since they are only 1/25 of a wavelength in thickness, when two sections are joined, they are fairly transparent to the impulse (16). As a crude approximation they produce 1/25 of the reflection that an infinite thickness of plexiglass would. Therefore, any reflection caused by these seals would probably be unnoticed as compared to the other reflections.

Attached to one end of the waveguide is an adapter that electrically connects the waveguide to coaxial cable while maintaining a constant diameter ratio, α, so as a propagating pulse will encounter no impedance change that would produce a reflection. However, at times the field was so large in the small part of the adapter, it broke down between conductors. In order to remedy the problem without building a new adapter, a teflon sleeve was inserted between the conductors. Because teflon breaks down at higher field strengths than air, the arcing was corrected. The teflon created a small discontinuity which will later be seen

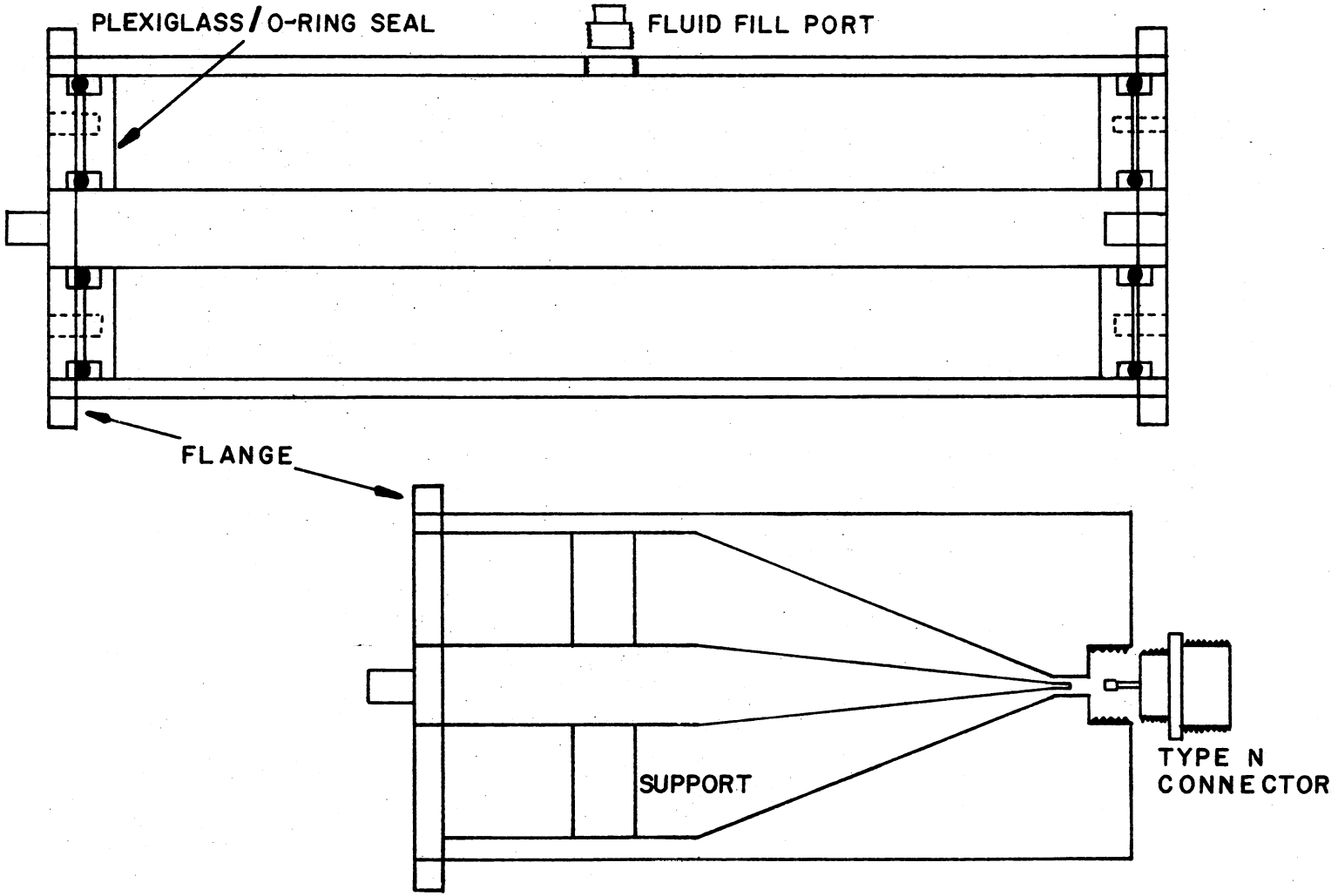

Figure 17. Coax Cable to Waveguide Adapter and Typical Waveguide Section

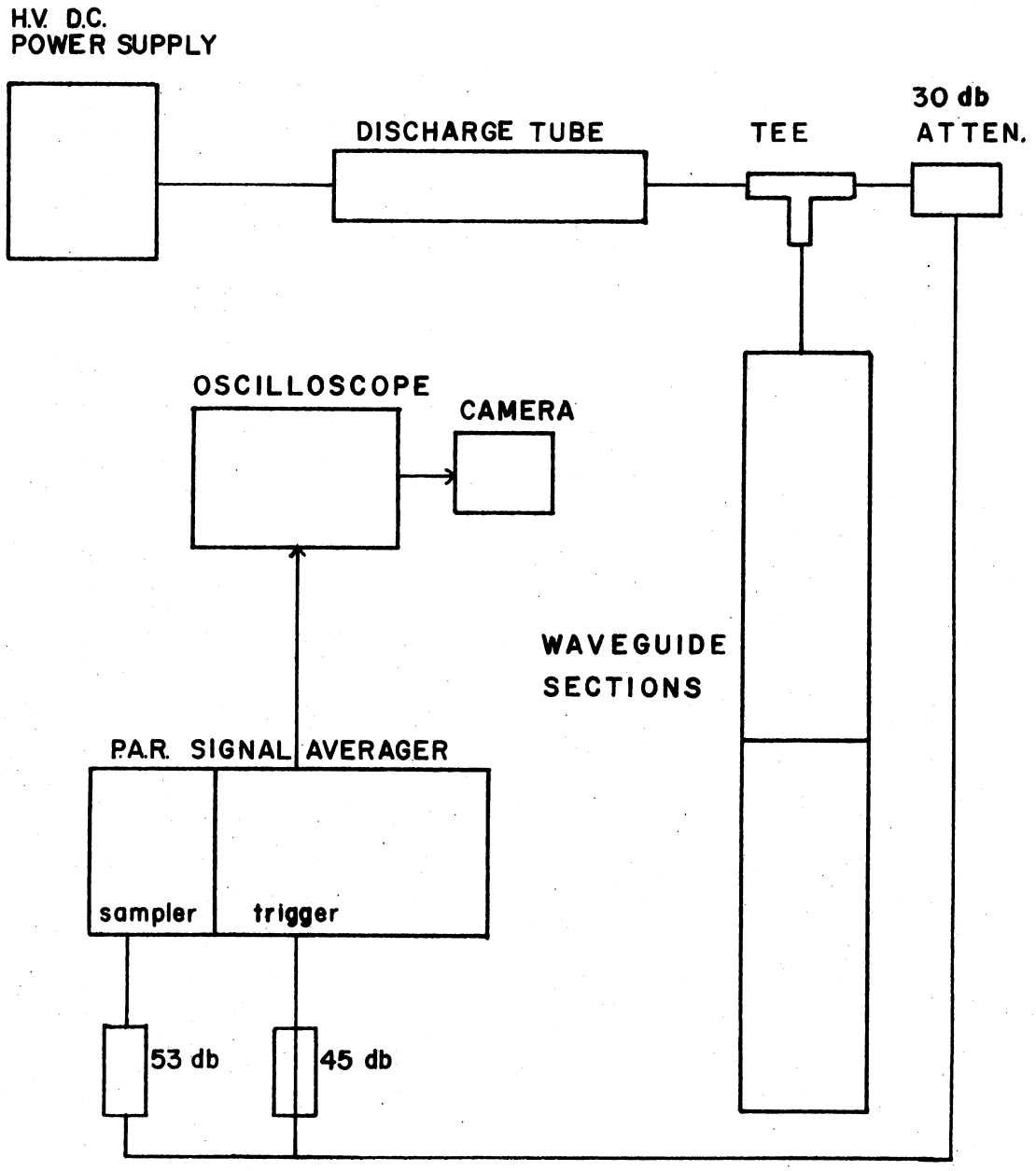

Figure 18. Waveguide, Source and Detector Configuration

in the data.

Figure 18 depicts the waveguide, source, and detection configuration. From this layout, the "tee" samples the incident pulse which serves as a trigger and time mark, from which the reflections can be measured in time. The interconnecting cables have been labeled as to their transit time:

$$t_{cable} = X_{cable}/v_{cable}$$

This was done in order to quickly isolate any discontinuities that might arise from faulty connectors which was a common occurrence.

Detector

The detector used was a P.A.R. Boxcar Integrator in conjunction with a Tektronix 75 picosecond risetime sampling head. The signal averaging properties of the integrator enabled noise and jitter to be averaged out resulting in a clean looking output, however, this was usually at the expense of resolution and/or sampling time. A compromise between noise reduction and sampling time resulted in a sample period of about 200 seconds and a real time sample range of 100 nanoseconds, and resolution of approximately 1 nanosecond. There was a slight amount of pulse broadening created by the averaging also.

The signal delivered to the detector had to be of a low voltage level, usually around 200 mv. This necessitated the attenuation of the signal from the waveguide by 83 db. The disadvantage of this is that the largest signal, the sampled incident pulse, had to be attenuated 83 db resulting in the reflected signals, which were smaller in amplitude, to be attenuated 83 db producing a loss of sensitivity for the

small reflections. What is needed is a pair of directional couplers or a circulator, however, obtaining a device to withstand such high field intensities in addition to being broadbanded, is difficult.

The delay line seen in Figure 19 is present in order to delay the signal arriving at the sampling head. A delay of 75 nanoseconds, with respect to the trigger signal, is due to the time required for internal mechanisms to cause the sampling head to sample. Since the trigger signal must be about 25 times larger than the sampled signal, a portion of the 83 db attenuation is located between the trigger input and the sampler head.

The output of the boxcar was fed to a Tektronix 5103 oscilloscope, however, since the output of one sweep took several minutes, a polaroid camera was used to make a permanent record of the trace.

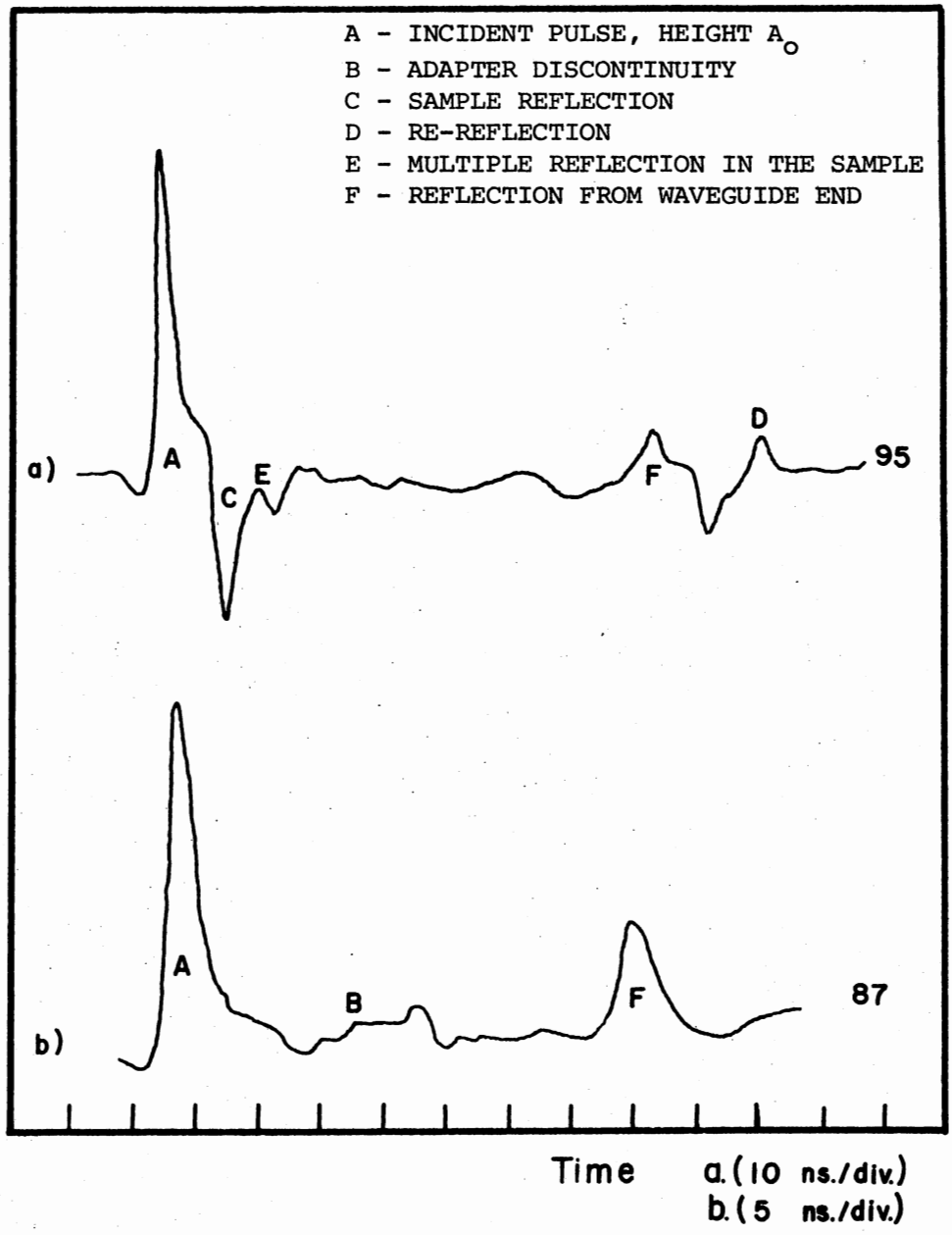

Figure 19. Typical Time Domain Reflectometer Data as Recorded From Oscilloscope

CHAPTER V

DATA ANALYSIS

As previously discussed and seen in Figure 18, the reflection coefficient measurement consisted of sampling the pulse in each arm, and the detection of any subsequent reflections from the waveguide. By comparing the reflection amplitude to that of the incident pulse, the reflection coefficient, R, may be deduced. One advantage of this method is, since a ratio is used, the amplitude of the incident pulse need not always be consistent.

Technique

The reflection coefficient of an interface in a multilayered system is not readily obtainable since the transmission coefficients of each previous interface need also to be known. These transmission coefficients may be obtained by analyzing each interface separately. Since the data is recorded on photographs, the accuracy of the ratios is limited. For the determination of a reflection coefficient from an interface several layers deep, the error in each, even though small, may result in a rather large discrepancy since the transmission coefficients are squred and multiplied together.

The alternative to reflection information was the time domain information where the time interval, Δt, between two consecutive reflections could be measured. Since the thickness of each section was known

the velocity could be determined, hence the dielectric constant by means of the equation on Page 26. Hypothetically, the reflections were replaced by delta functions located at the times of maximum amplitudes of the reflections, which, for dispersionless samples, the two way time of flight was the difference between two consecutive delta functions. An example of Δt is shown in Figure 19, which depicts a typical time domain output of the detector. This method of characterization of the samples proved to be quicker and more accurate than the reflection coefficient method. The two methods compare quite well as will be seen in the data.

A problem in this reflectometer design, is the use of a nondirectional "tee" instead of a circulator or directional couplers, the reflections produced in the waveguide may be reflected. This occurs when the reflections arrive at the "tee". They are not only directed to the detector, but also back to the source. Empirically it is seen that since the discharge tube maintains a constant 50Ω impedance, it doesn't appear as a discontinuity, aside from the gaps. The reflections directed into the source arm propagate back to the H.V. power supply where they encounter the low impedance of the capacitor, C_1. In terms of impedances, the reflection coefficient R is:

$$R = \frac{Z_1 - Z_2}{Z_2 + Z_1}$$

In traveling from a high impedance to a low, the coefficient is negative, indicating a phase reversal of the pulse. This is what occurs at the power supply and the reflections are redirected back to the "tee", hence, detector. The problem did not interfere with the measurements. The coaxial line that supplied power to the discharge tube was sufficiently long such that any re-reflections were far enough in time

away from the primary reflections to be of no concern. Point "D" in Figure 19 is the first arrival of a re-reflection and can be seen to be over 100 ns away from the incident pulse.

Also in this figure the incident pulse, a reflection from a sample, and the reflection from the end of the waveguide can be noted.

Calibration of the System

Before any valid data could be taken, the reflectometer had to be calibrated for both the amplitude and time of flight measurements, also, the time base and amplification sections of the detector had to be checked for linearity.

The first step was to determine in time, with respect to the "tee", where the various components of the waveguide were located (15). This was accomplished by locating the end of the guide when it contained (a) only the coax-line to waveguide adapter, (b) only one waveguide section, and (c) both sections. This is shown in Figure 20 and plotted in Figure 21, where zero time is the location of the "tee". The plot of distance versus Δt defines the velocity of the pulse. For an air-filled guide v should be c (3.0×10^8 m/sec). The curve in Figure 21 agrees with this and from its linear shapes suggests the detector has a linear time base.

Also seen in Figure 20, there appears to be a slight discontinuity at the adapter. This was expected as discussed in Chapter IV due to the insertion of the teflon shield to prevent breakdown in the adapter. From an amplitude calculation, this discontinuity can be treated as an interface of zero thickness, possessing a reflection coefficient of .10, thus a transmission coefficient of .90.

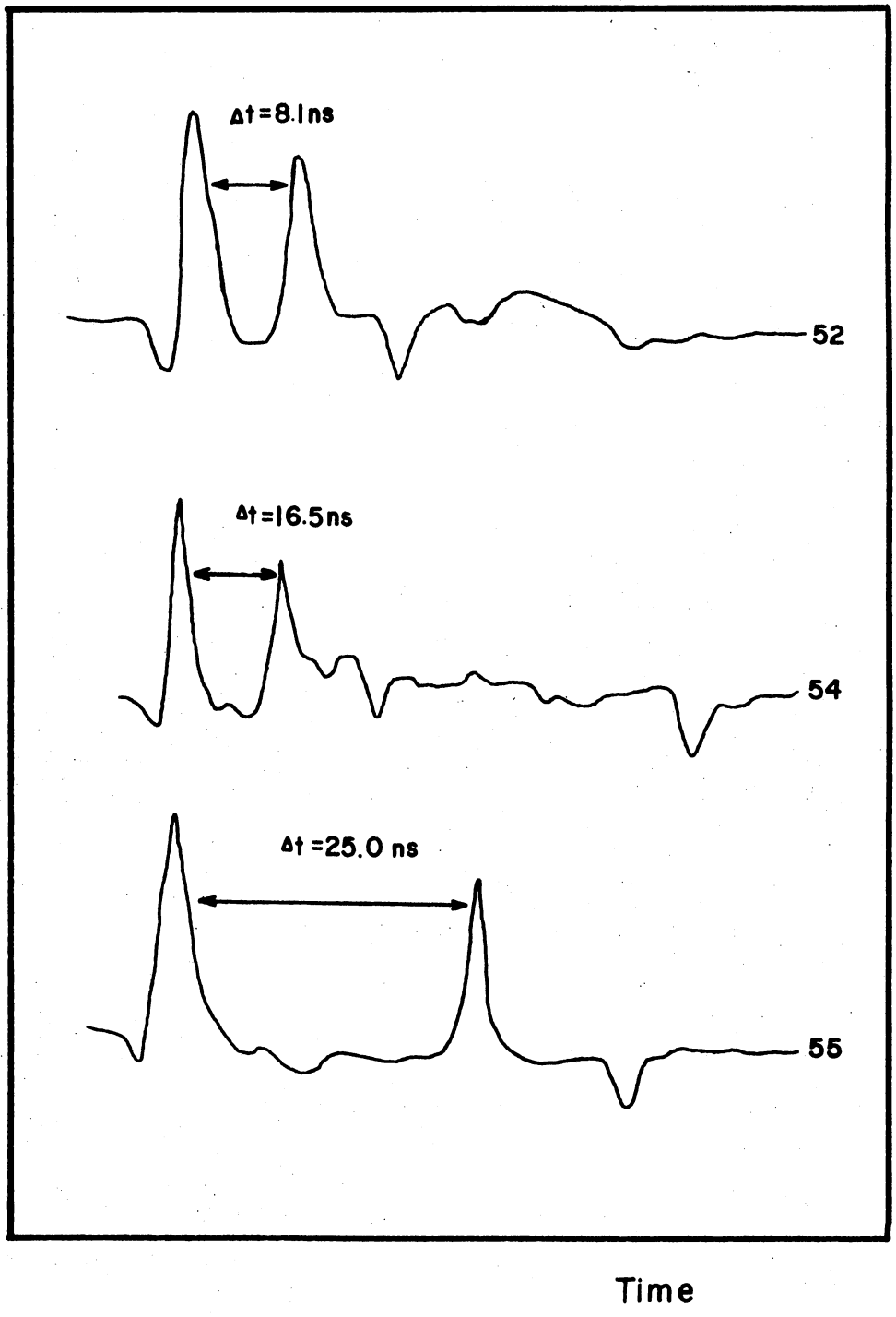

Figure 20. Time Domain Calibration of Reflectometer:
a) Adapter Only; b) One Air Line;
c) Two Air Line

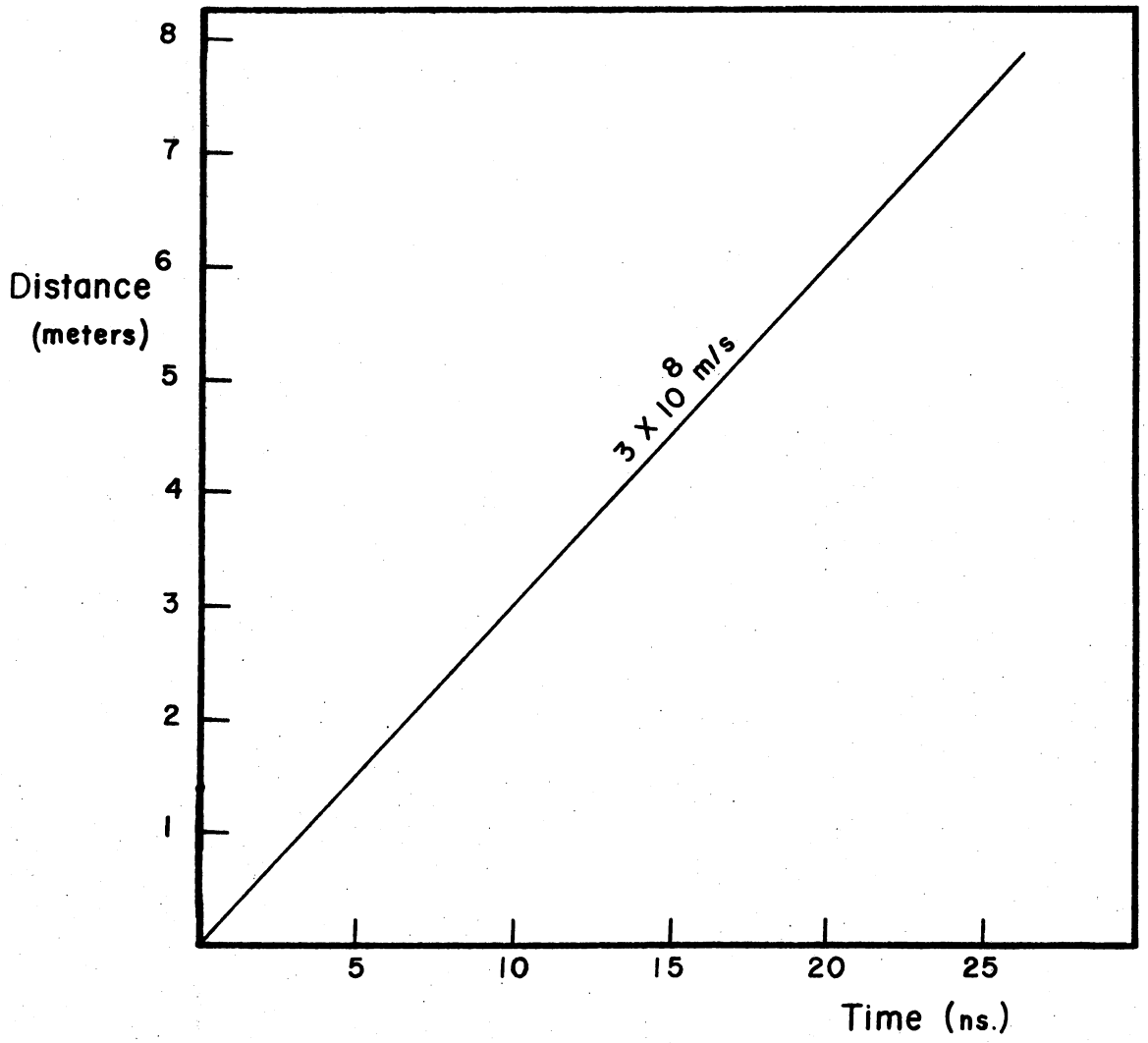

Figure 21. Time Domain Calibration; Linearity of Detector

Denoting these coefficients by R_a and T_a respectively, the amplitude of a reflection from the end of the waveguide may be predicted and compared to Figure 20 in order to check the linearity of the detector amplification. The ratio of this reflection to that of the incident pulse, A_{end}/A_o should be:

$$A/A_o = (T_a)^2 R_{end}$$

where R_{end} in terms of the 50Ω waveguide impedance and the 377Ω impedance of free space is:

$$R_{end} = \frac{Z_{F.S.} - Z_{W.G.\ end}}{Z_{F.S.} + Z_{W.G.\ end}} = \frac{377-50}{377+50}$$

thus,

$$A/A_o = (.90)^2(.77) = .62$$

which compares favorably to the value of .60 in Figure 20.

Another method of calibration was the use of a standard dielectric sample placed in a waveguide section. The standard had to be lossless, preferably liquid, and available in gallon size quantities; cyclohexane appeared to be well suited since it was a recommended reference dielectric with $\varepsilon_r = 2.0250$, however, due to its extreme flammability it was hazardous to work with.

With the first waveguide section filled with cyclohexane, the air-cyclohexane interface should have a reflection coefficient of:

$$R_{air\text{-}cyclo} = \frac{\sqrt{\varepsilon_{r\ cyclo}} - \sqrt{\varepsilon_{r\ air}}}{\sqrt{\varepsilon_{r\ cyclo}} + \sqrt{\varepsilon_{r\ air}}} = .17$$

Thus the detected amplitude from the first interface should be:

$$A/A_o = (T)^2 R = (.9)^2(.17) = .14$$

and for a sample length of 1.20m, the two way time of flight should be:

$$\Delta t = \frac{\sqrt{\varepsilon_r \cdot 2 \cdot x}}{c} = 11.4 \text{ ns}$$

both of which compare to the experimental values as seen in Figure 20.

By using these two methods of dielectric determination the experimental data may be verified since each method is independent of the parameters that determine the other.

Data Analysis

In order to always include the dielectric standard in the data, the first waveguide section was filled with cyclohexane and the second section with the sample material. In doing this, the time interval between the reflections from the ends of the cyclohexane is known to be 11.4 ns, and may be used as a time reference to subsequent reflections regardless of any error in the time base as long as it is linear.

An example of this may be seen in Figure 22 using distilled water as the sample in the second section. In this case, Δt of the reflections from the first water interface and end of the waveguide is 5.6 times the Δt for the cyclohexane, thus Δt water = 63.8 ns, corresponding to a dielectric constant of $\varepsilon_r = 71.1$ for water. This may also be checked by the detected amplitudes of reflections from the cyclohexane-water interface and the water-free space interface:

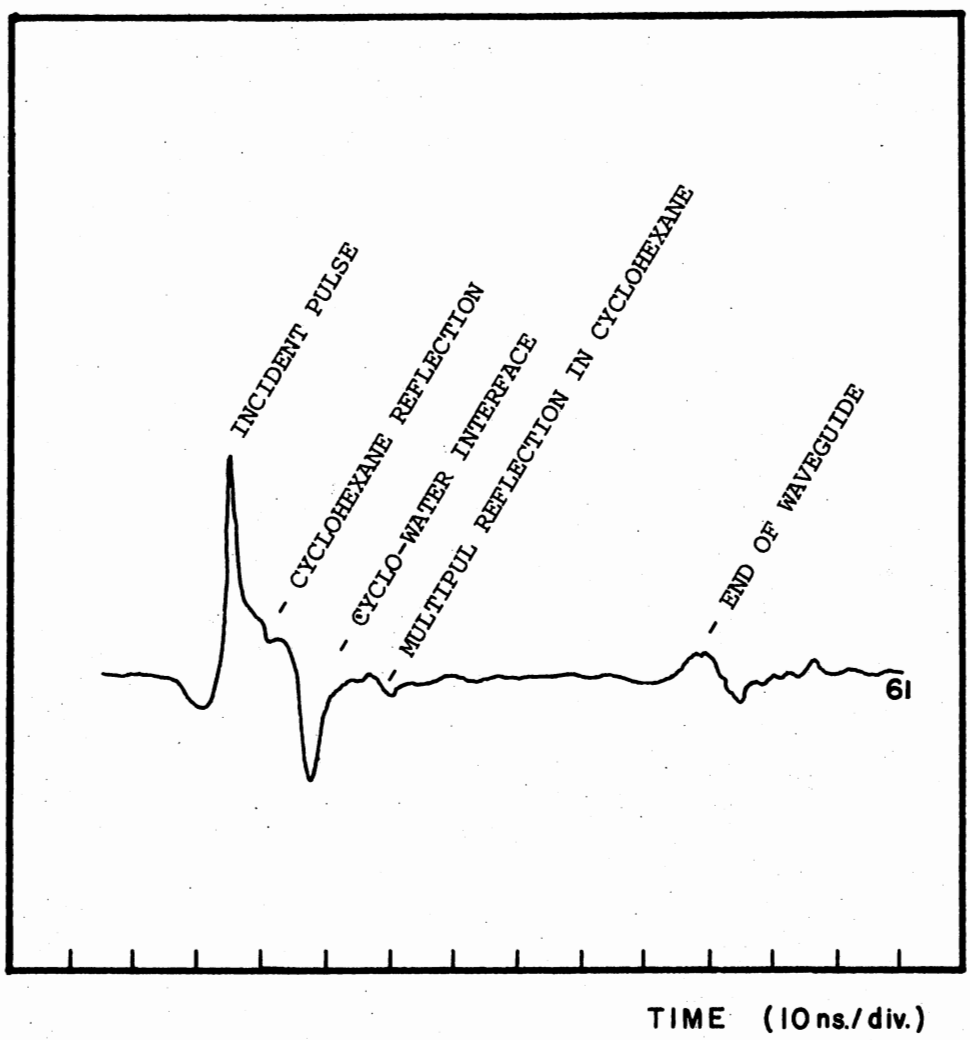

Figure 22. Cyclohexane as a Time Reference for the Determination of the Dielectric Constant of Water

$$\frac{A_{cyclo\text{-}H_2O}}{A_o} = (T_a)^2 (T_{air\text{-}cyclo})^2 (R_{cyclo\text{-}H_2O})$$

$$\frac{A_{H_2O\text{-}freespace}}{A_o} = (T_a)^2 (T_{air\text{-}cyclo})^2 (T_{cyclo\text{-}H_2O})^2 (R_{H_2O\text{-}freespace})$$

Solving the above equations for ε_{H_2O} and when using the detected amplitude ratios from Figure 22, the dielectric constant determined in this manner is in agreement with that predicted by the time of flight method. For example, solving for ε_r in terms of the detected reflection amplitude from the cyclohexane-water interface produces an equation as:

$$\varepsilon_{H_2O} = \varepsilon_{cyclo} \left[1 - \frac{A/A_o}{\left(T_a \, T_{air\text{-}cyclo} \right)^2} \right]^2 \left[1 + \frac{A/A_o}{\left(T_a \, T_{air\text{-}cyclo} \right)^2} \right]^{-2}$$

and for A/A_o of .385, ε_{H_2O} appears as 64.1.

A further example of this is seen in Figure 23 using crude oil. Only one section was used (no cyclohexane); the time of flight yields $\varepsilon_r = 2.21$ and the amplitudes yields $\varepsilon_r = 2.65$.

It must be noted that at times the two methods may not agree. If this occurs, then the dielectric constant may be suspected of being a complex function resulting in an amplitude attenuation, whereas the velocity may only change slightly.

An experiment that was done using the reflectometer was to determine how the electrical parameters of a terrestrial media change when intruded with water. Two porous materials were used; a fine grained sand with an average grain size of .075" and diatomaceous earth with a particle size of the order of microns. Distilled water was introduced to these samples in varying amounts, and the associated change in the

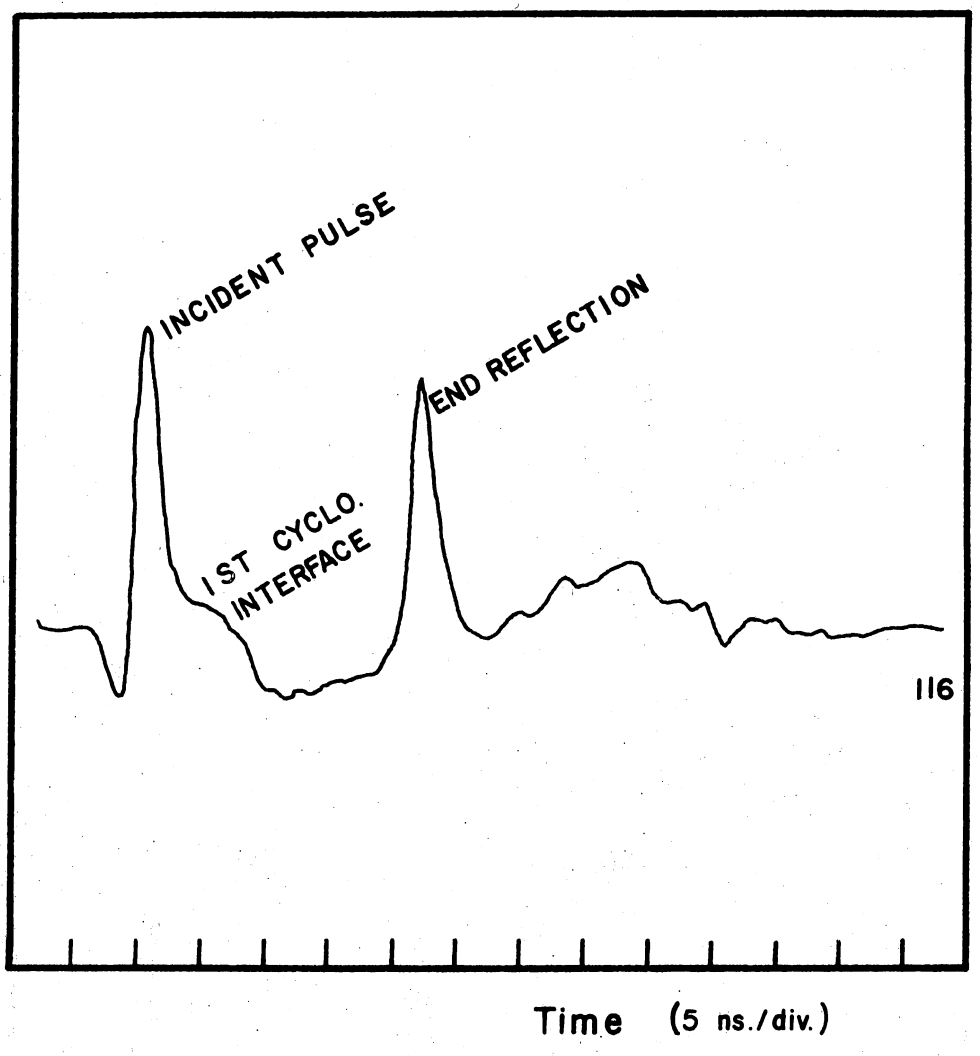

Figure 23. Determination of ε_r of Crude Oil Using Amplitude and Time of Flight Methods

dielectric constant was noted.

It was hypothesized that when the surface area of the porous sample is so large that the water is electrostatically bonded to the surface of each particle in the form of layers only several molecules thick, the dipole motion of water is hindered, hence the dielectric constant of the mixture will not indicate the presence of the water as it would if the water is free. When the amount of water added is greater than that needed to coat all the particles, then it appears as free water in the pore space and the dielectric constant is affected by it.

To begin with, each sample was prepared by an extended washing in order to remove any free mineral salt deposits so that the conductivity doesn't erroneously rise when water is added. Next, the samples were rinsed in acetone and then the acetone boiled off in order to remove any traces of water, after which they were placed in a vacuum.

The measurements consisted of beginning with the completely dry sample and determining ε_r from the amplitude and time of flight method. Then, the sample was removed and varying amounts of water were added to the sample after which it was replaced in the waveguide and ε_r determined again. By comparing ε_r calculated by both methods, any attenuation present would be apparent, however, as seen in the data tables none was for either sample. In Figure 24 are typical traces for the sand-water and diatomaceous earth-water mixtures. Since it was more accurate to measure Δt between the incident and end reflected pulses due to their well defined peaks, the time interval of the sample, Δt_s could be determined since it was previously determined that the "tee" was 19.5 ns away from the end of the cyclohexane section, thus:

$$\Delta t_s = [\Delta t - 19.5]\text{ns}$$

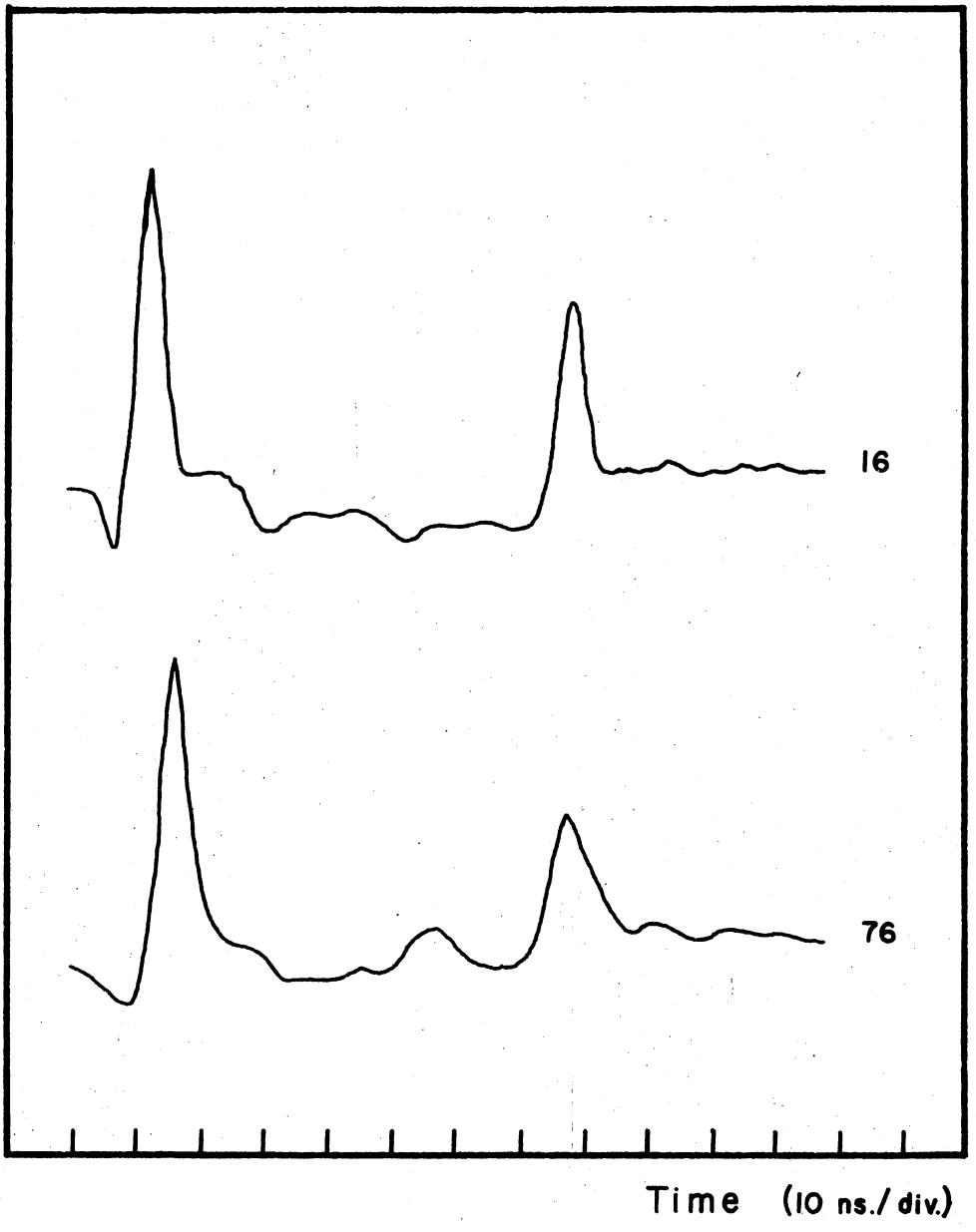

Figure 24. (a) Cyclohexane and Sand Data
(b) Cyclohexane and 2% H_2O-Diatomaceous Earth Data

Data tables I and II denote the increase in dielectric constants with the increase in water content. Water was added until the percentage of it was so great that the mixture began to separate. This is apparent in the sand-water mixtures for water content higher than 10%. Figure 25 plots the dielectric constant versus the water content for sand while Figure 26 plots the same for diatomaceous earth.

Perhaps a more practical aspect of these results is the differentiation between fluid impregnated and non-impregnated terrestrial materials. Several examples of how this concept may be applied are; determination of the location of the ground water table, the differentiation between sand, containing no fluid, containing hydrocarbons, or being water bearing.

An experiment was done in order to test the practicality of this method. Since the dielectric constants have been previously determined for water bearing sand, the ability of the reflectometer to distinguish dry sand from hydrocarbon bearing sand will be attempted.

To do this, half of a waveguide section was filled with dry sand. On top of this, the other half was filled with a saturated mixture of crude oil and sand. Figure 27 represents a cross sectional view of the waveguide section. By weight, the oil sand mixture contains 25% oil and 75% sand. The dielectric constant for both substances had previously been determined to be 1.89 for sand and 2.21 for crude oil. The resulting mixture should possess a dielectric constant of 1.97, calculated by the mass ratio method.

The interface between the dry sand and the oil sand should have a reflection coefficient of:

$$\frac{A}{A_o} = (T_a)^2 (T_{\text{air-sand}})^2 (R_{\text{sand-oil sand}})$$

TABLE I

DIATOMACEOUS EARTH-WATER MIXTURES

% H_2O by Wt.	Time of Flight Δt	ε_r Cal. From Δt	A/A_o Predicted	Actual A/A_o	Photo Number
0	10.0	1.56	.62	.60	75
.09	10.5	1.72	.60	.58	76
3.9	11.5	2.07	.54	.50	77
5.6	12.5	2.44	.50	.50	79
7.4	13.5	2.85	.46	.52	78
9.1	12.5	2.44	.50	.50	80
10.7	12.5	2.44	.50	.51	81
13.8	13.5	2.85	.46	.46	83
20.0	13.5	2.85	.46	.48	82
23.1	13.5	2.85	.46	.46	84
28.6	15.5	3.75	.39	.37	85
33.3	16.5	4.25	.37	.32	88
41.2	20.5	6.57	.28	.20	86
45.9	24.5	9.38	.22	.23	89
51.2	27.5	11.82	.19	.18	91
55.6	33.5	17.54	.14	.13	90
100.0	64.4	81.1	.05	.013	61

TABLE II

SAND-WATER MIXTURES

% H_2O by Wt.	Time of Flight Δt	ε_r From Δt	Predicted End Reflection	Actual End Reflection	Photo Number
0	11.0	1.89	.57	.56	18
1.9	14.8	3.42	.42	.40	20
3.6	15.0	3.52	.41	.39	25
5.3	17.0	4.52	.35	.38	30
7.0	17.5	4.79	.34	.34	29
8.6	19.0	5.64	.31	.31	31
11.6	24.0	9.00	.23	.25	33
15.8	27.5	11.82	.19	.17	38
100.0	64.4	81.1	.05	.013	61

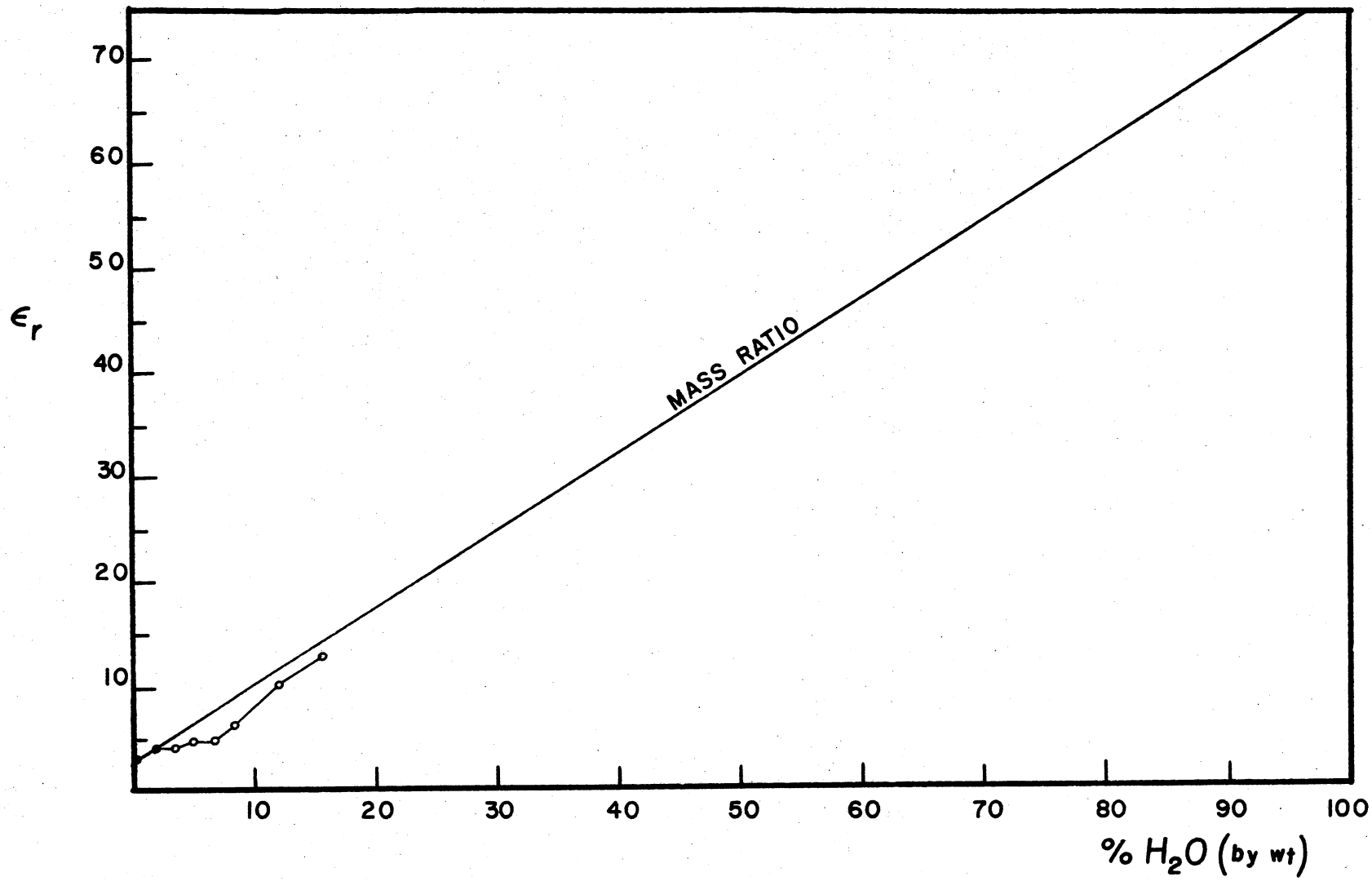

Figure 25. The Dielectric Constant of a Water-Medium Grained Sand Mixture as a Function of Water Content

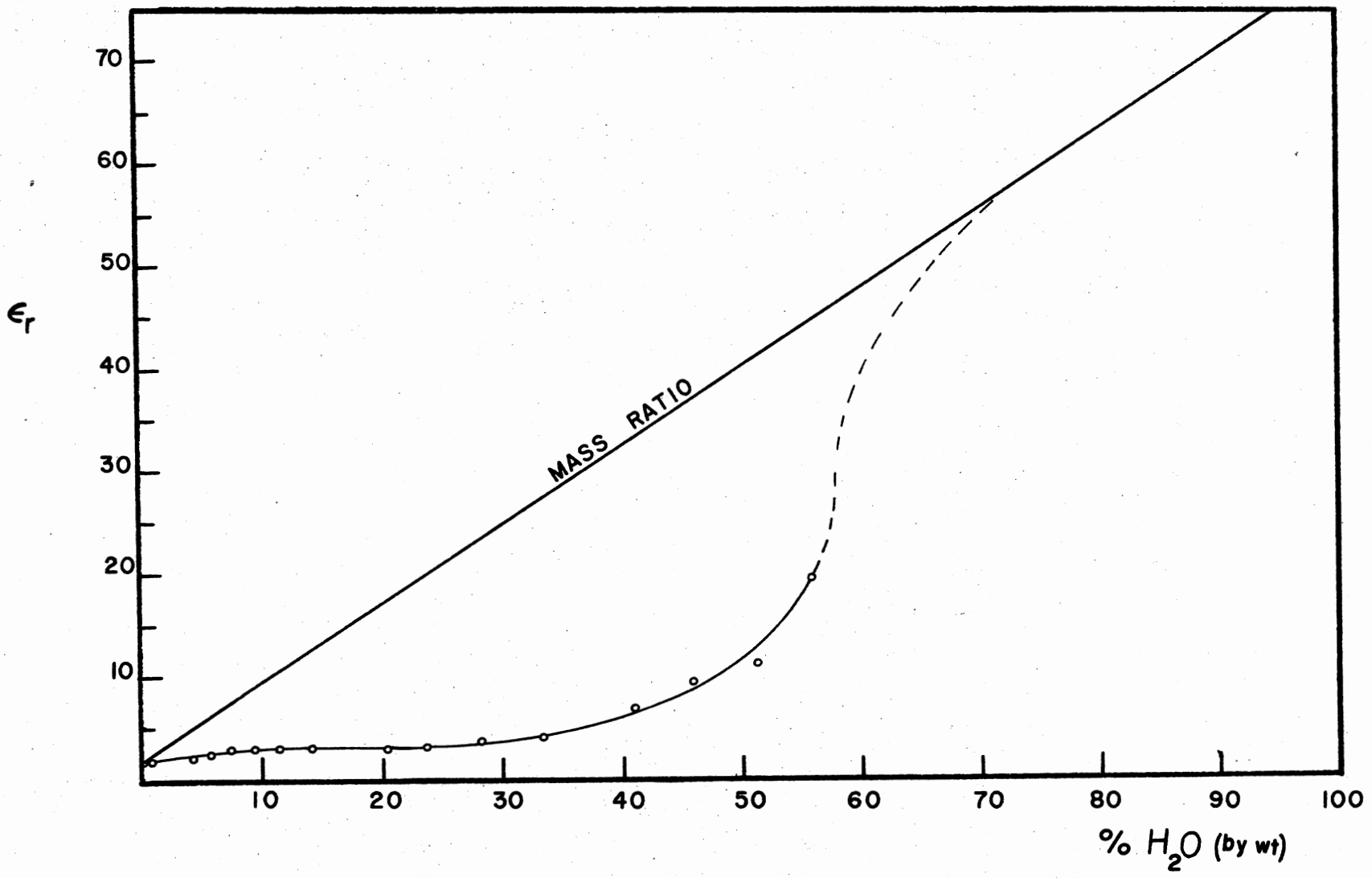

Figure 26. The Dielectric Constant of a Water-Diatomaceous Earth Mixture as a Function of Water Constant

The time domain reflection data is depicted in Figure 28, where point B is the reflection generated by the pulse incident upon the oil sand. Taking into account the adapter discontinuity, this reflection has a detected magnitude relative to the incident pulse of .014. This agrees very well with the predicted value of .010.

Lossy Media

The natural limiting feature of subsurface impulse propagation is the amount of dissipation present. The dissipation is represented by the imaginary portion of the dielectric constant, which, is dependent upon the conductivity and frequency. The net effect of the dissipation is termed the attenuation. As mentioned in Chapter II, the complex wave number is:

$$k^2 = \frac{\mu\varepsilon_r\omega^2}{c^2}\left(1 + \frac{i4\pi\sigma}{\omega\varepsilon_r}\right)$$

where the second term represents a conduction current or dissipation. Taking the square root of k and utilizing the physically meaningful branch, for a good conductor, $\frac{4\pi\sigma}{\omega\varepsilon_r} >> 1$ and,

$$k \approx (1+i)\left(\frac{2\pi\omega\mu\sigma}{c}\right)$$

and for a poor conductor $\frac{4\pi\sigma}{\omega\varepsilon_r} << 1$ and;

$$k = \sqrt{\mu\varepsilon_r}\ \frac{\omega}{c} + \frac{i2\pi}{c}\sqrt{\frac{\mu}{\varepsilon_r}}\ \sigma$$

Any conductivity associated with terrestrial media will usually, except under peculiar situations, comprise the definition of being a

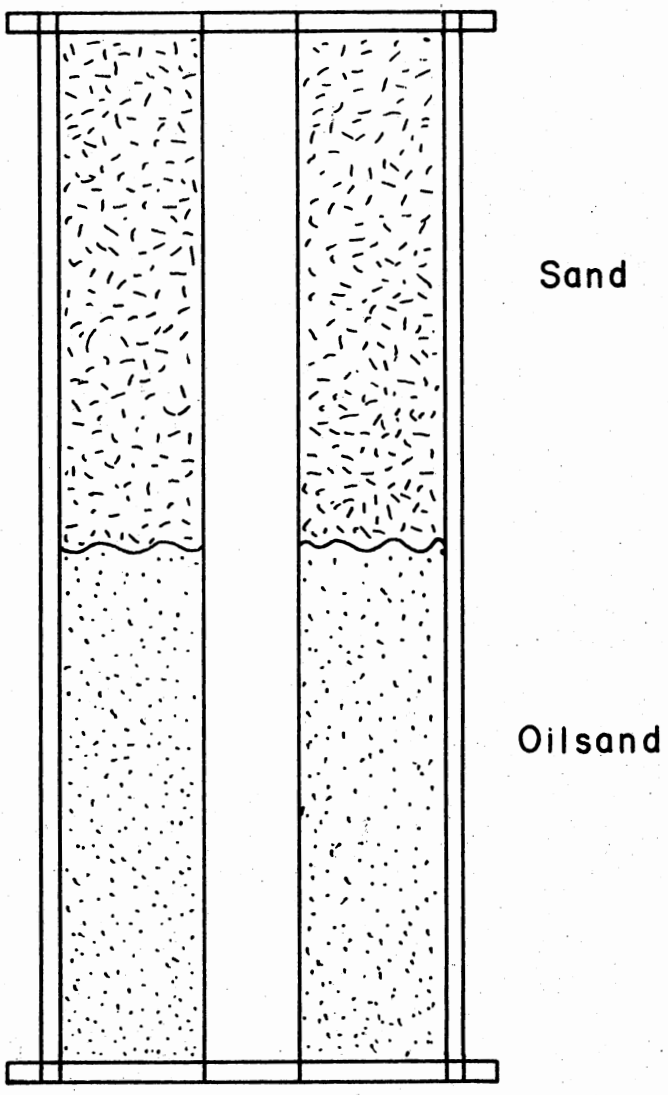

Figure 27. Sand-Oilsand Configuration in Waveguide Section

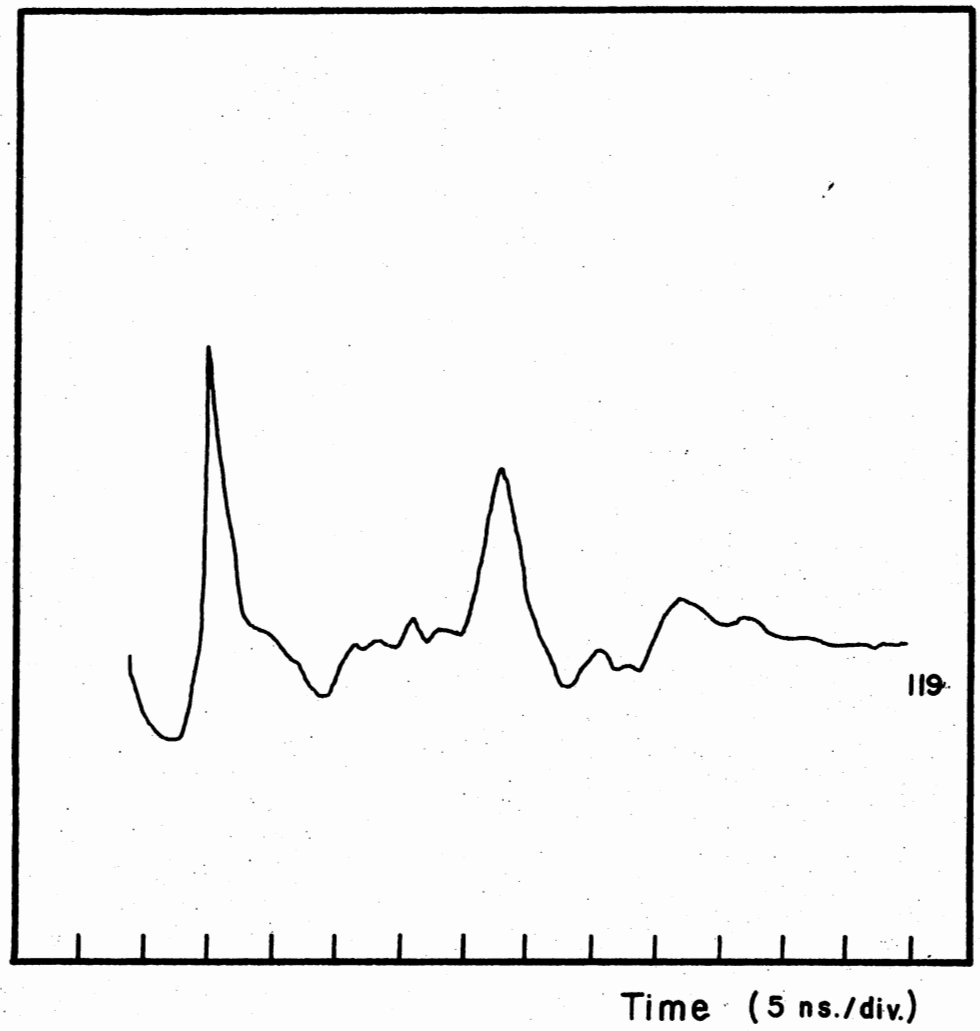

Figure 28. Sand-Oilsand Data

poor conductor (8). For the majority of the frequency components of the impulse, and since $\sigma \simeq 1.0$ mhos, the condition, $\frac{4\pi\sigma}{\omega\varepsilon_r} << 1$ is satisfied.

Using the poor conductor expression, the attenuation coefficient is independent of frequency:

$$\alpha = \frac{4\pi}{c}\sqrt{\frac{1}{\varepsilon_r}}\,\sigma\left[\frac{\text{nepers}}{\text{m}}\right]$$

and only dependent upon the conductivity.

It was desireable to estimate what order of magnitude attenuation the impulse would experience in the lossiest subterrainian media. Most certainly the largest contributor to the attenuation would arise from mineral salts being dissolved in water (12). Before the attenuation coefficient could be predicted from the poor conductor expression, a knowledge of the conductivity of water as a function of salt content had to be established.

This was empirically determined by dissolving the salt, sodium chloride in water and measuring the conductivity. Two electrodes were placed in the solution and using an ohm meter, the resistance was measured. Since the resistance is simply the reciprocal of the conductivity, σ could readily be determined. Although the use of an ohm meter and two electrodes is not an accurate method for quantitative data, it was sufficient for the description of the general behavior of σ versus NaCl concentration.

Figure 29 shows the conductivity as measured by this method. As can be seen, the conductivity is extremely sensitive to small concen-

trations of salt. However, it rapidly becomes asymptotic to a constant value for the conductivity. Once this value is reached, the conductivity is oblivious to any further increases in concentration, even to the saturation point.

This rather unexpected behavior may be explained by the Debye-Hückel theory ionic clouds around ions of opposite polarity. These clouds, under the influence of an electric field, hinder the movement of ions; an apparent increase in viscosity is observed. Figure 30a shows an ionic cloud of chlorine ions centered about a sodium ion, while Figure 30b is the cloud under the influence of an electric field.

When the salt concentration is small, the density of dissociated ions if so small, the clouds are not able to form completely. Hence, for small ion densities, the conductivity will increase as the ion density increases. When the density of ions is great enough, the ion clouds readily form and the apparent conductivity is due only to the mobility of the clouds. As the salt concentration is increased further, more clouds form and the conductivity remains constant.

This knowledge of the conductivity enables a determination of α as a function of salt concentration. Figure 31 plots the attenuation coefficient as a function of salt content in water. This plot was derived from the expression for α in a poor conductor.

In order to experimentally verify this curve, the impulse was propagated through a waveguide section containing various amounts of salt dissolved in distilled water. Since the attenuation coefficient for distilled water is essentially zero, the attenuation for salt water could be determined by a ratio of the end reflection amplitudes.

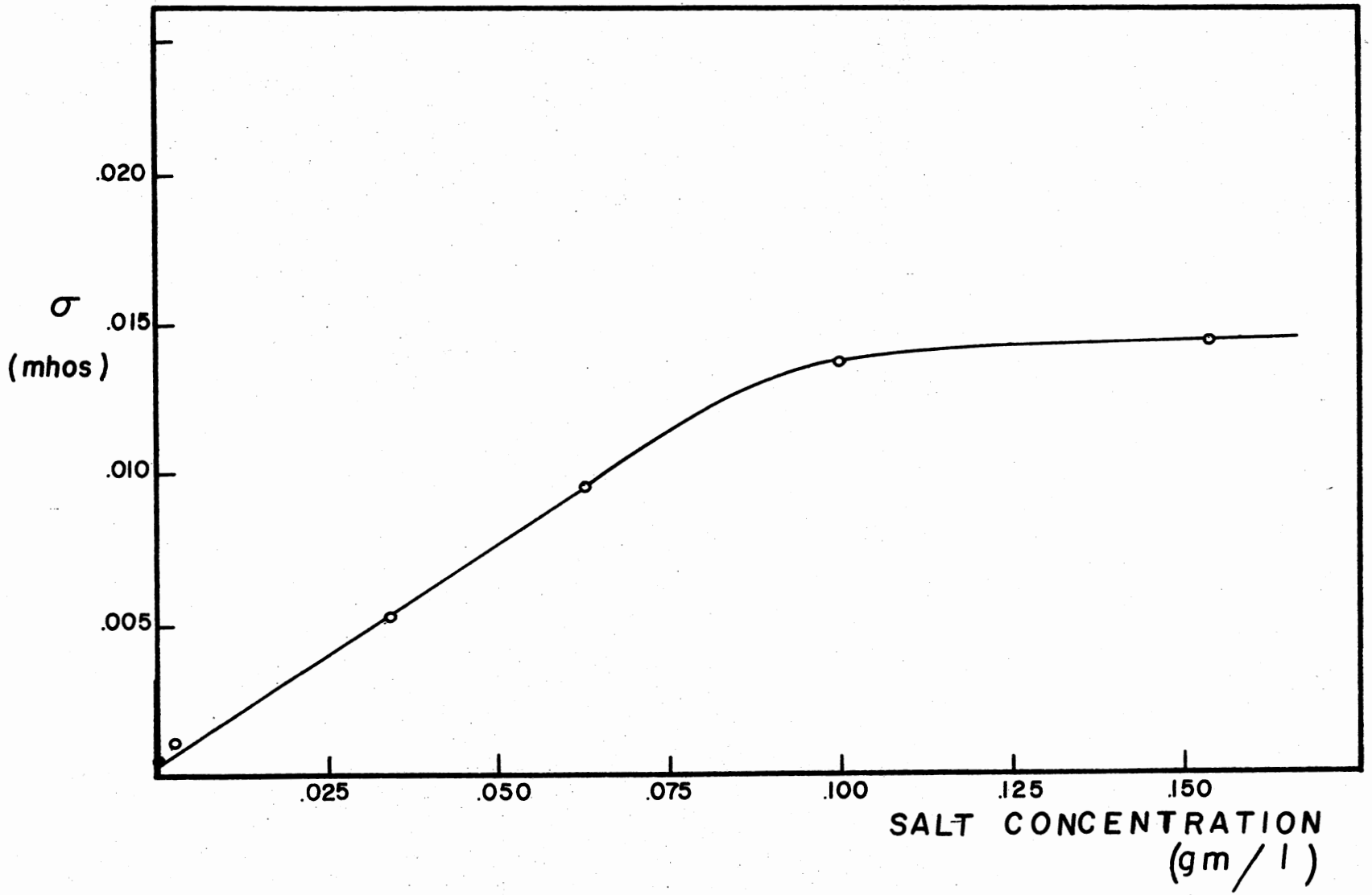

Figure 29. Conductivity of Salt Water as a Function of Salt Concentration

This relationship may be derived in the following manner:

1) for distilled water the detected end reflection has an amplitude of:

$$\frac{A_{end\text{-}dw}}{A_o} = (T_a)^2 (T_{air\text{-}H_2O})^2 (R_{end})$$

2) for salt water:

$$\frac{A_{end\text{-}sw}}{A_o} = (T_a)^2 (T_{air\text{-}H_2O})^2 (R_{end})\ e^{-2\alpha x}$$

A ratio of the two,

$$\frac{A_{end\text{-}dw}}{A_{end\text{-}sw}} = e^{2\alpha x}$$

From this alpha may be determined:

$$\alpha = \frac{1}{2x} \ln \left(\frac{A_{end\text{-}dw}}{A_{end\text{-}sw}} \right)$$

The results of this experiment are plotted in Figure 31 along with the calculated attenuation coefficient.

Dispersion

The only samples that displayed any impulse broadening properties were the salt water solutions. The degree of broadening was dependent upon the amount of salt dissolved in the water.

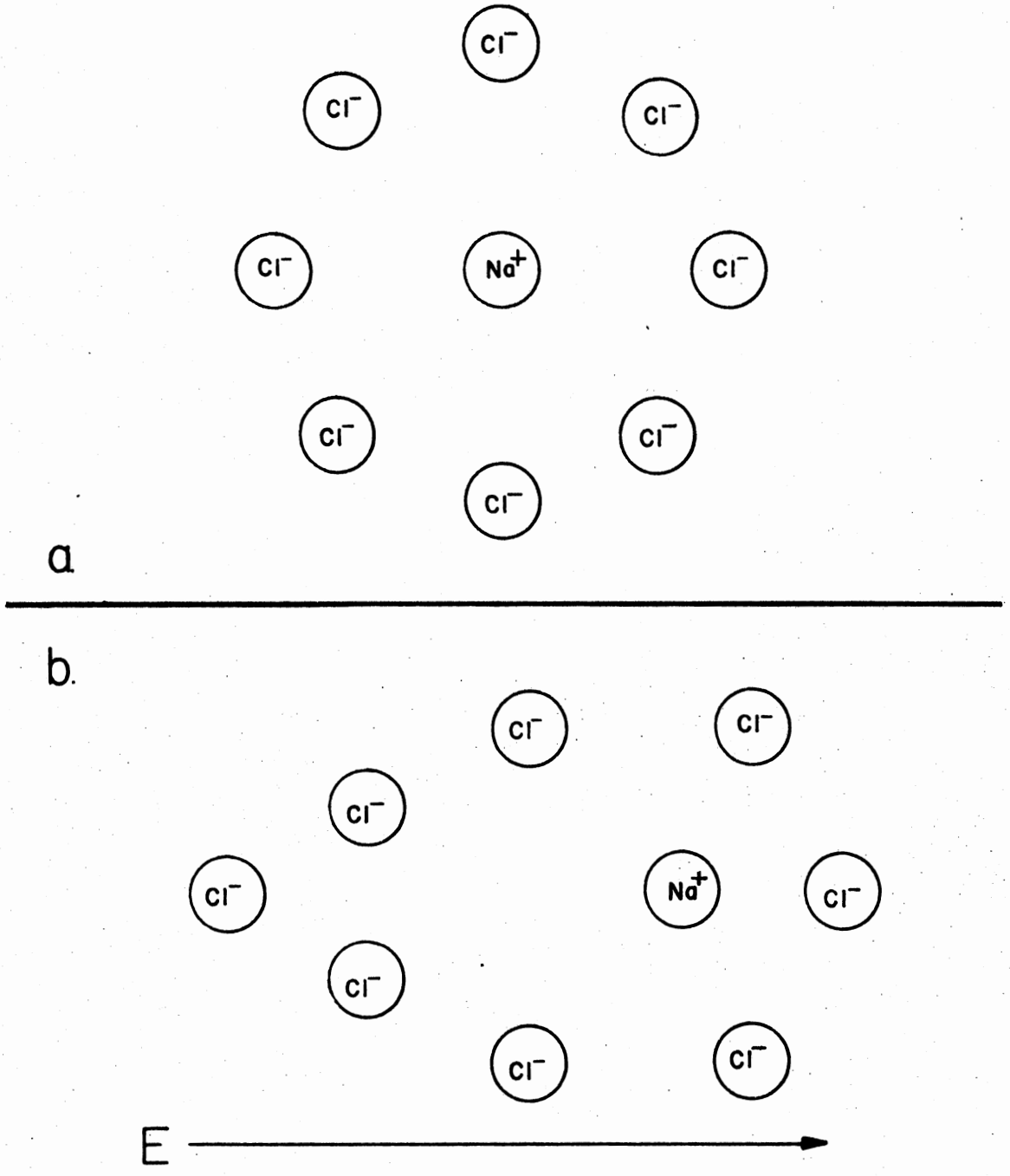

Figure 30. Debye-Hückel Ionic Cloud: (a) No Electric Field Present; (b) Under the Influence of an Electric Field

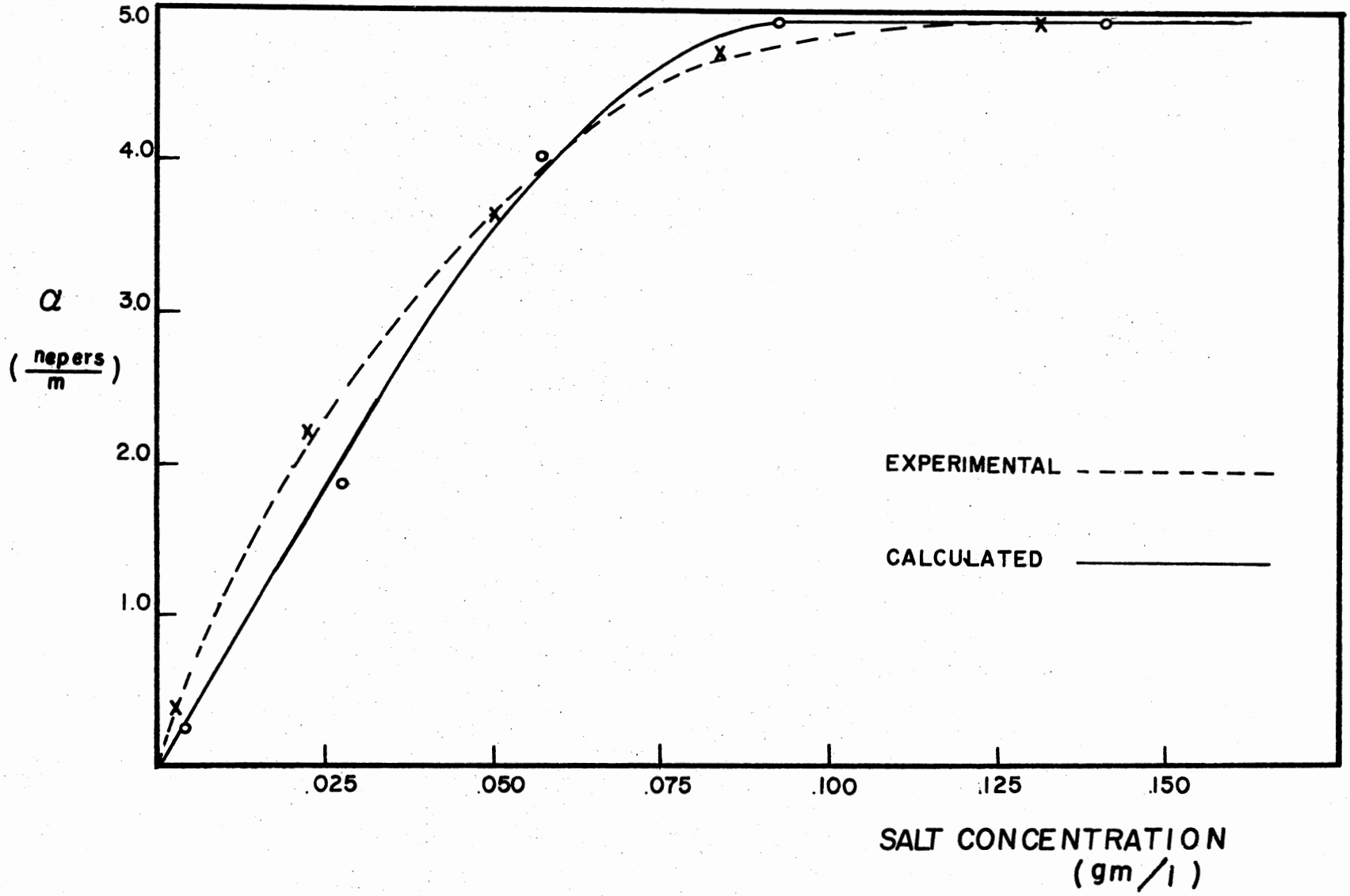

Figure 31. Experimental and Predicted Values of the Attenuation Coefficient

Any spreading of the impulse cannot be the result of frequency dependent absorption since this would only cause an amplitude distortion. Dispersion is most likely the source of the broadening. This is in agreement with the effect that normal dispersion has upon a sharp pulse. An example of this is seen in Jackson (10).

CHAPTER VI

CONCLUSIONS

The feasibility of the use of electromagnetic waves as a remote sensing device is by no means deemed unacceptable by this research. The natural limitation of such a method appears to be the amount of attenuation the earth presents to a propagating wave. Most subsurface material, when deprived of any moisture content, act as typical lossless dielectrics. Any attenuation has been found to arise mainly from the amount of mineral salts dissolved in any water present. The amount of salt concentration, hence, conductivity, determines the attenuation coefficient. Fortunately simple salts such as NaCl have a finite limit to the conductivity when in solution. This limit may be explained by the Debye-Hückel theory and has been found to have a maximum conductivity corresponding to a 5 nepers/m maximum attenuation for salt-water.

An interesting effect upon the dielectric constant was noticed when nonconducting water was introduced into various media. It was found that the dielectric constant of the mixture had a value corresponding to the mass ratio of the two constituents for most materials. However, for porous samples which had a large surface area due to the small pore size, this mass ratio relation could no longer predict the dielectric constant. It appears that when the water concentration is low enough, most of the water is surface bonded to the pores and little free water remains. This bonding inhibits the polarization process

resulting in a lower than expected value for ε_r. This effect is not noticed until pore sizes of the order of microns are encountered. Most sandstones have large enough pores to exclude this effect but it may be noticed in such materials as siltstones, diatomaceous earths, and some clays.

The most favorable approach to electromagnetic subsurface surveying is utilizing a broadband impulse. By time of flight analysis and the use of other than normal incidences, interfaces of strata may be spatially located. Even in the presence of attenuation this method is not hindered since it is independent of amplitude analysis. The depth of penetration is limited by the attenuation, however.

In order to achieve a spatial resolution of a few feet, an ultrashort impulse had to be used as the source. In addition, the impulse had to be of a high power level. Such a device was constructed using dual spark gaps in a coaxial waveguide capable of 1 ns impulse at 3 KV. The device was characterized sufficiently to understand the basic principals of its operation, however, its complex nature is readily apparent.

The broadwidth of the impulse produced was over 1 GHz wide. With a pulse this large in frequency, components dispersion could have a highly distortive effect. For all of the lossless terrestrial materials investigated, no dispersion or resonant absorptions could be noticed. Only in lossy media was any impulse distortion apparent. Since most terrestrial conductivities are low enough to be considered poor, the attenuation is only dependent upon the conduction currents. Any distortion must therefore be due to the frequency dependence of the conductivity.

Further research in this area should include electromagnetic wave propagation and information transportation through highly dissipative materials. Such methods may be the use of convolution and correlation. The gas discharge tube used to produce the impulse could also be the subject of further study.

A SELECTED BIBLIOGRAPHY

(1) Arfken, G., Mathematical Methods for Physicists, 2nd ed.: New York, Academic Press (1970).

(2) Cook, J. C., J. Expl. Geoph. 40, 5 (1975).

(3) Craggs, J. D. and J. M. Meek, Electrical Breakdown of Gases: Oxford, Clarendon Press (1953).

(4) Diefenderfer, A. J., Principals of Electronic Instrumentation: New York, Saunders (1972).

(5) Encyclopedia of Physics, Vol. 21. Electron Emission and Gas Discharges I: Berlin, Springer-Verlag (1956).

(6) Encyclopedia of Physics, Vol. 22. Electron Emission and Gas Discharges II: Berlin, Springer-Verlag (1956).

(7) Heard, H. G., Rev. Sci. Instr. 25, 5 (1954).

(8) Holdsworth, D. W. and A. R. Barringer, "Studies of the Radar Properties of Rocks in a Vacuum," Barringer Research Inc., Mass.

(9) Howatson, A. M., An Introduction to Gas Discharges, 1st ed.: London, Pergaman Press (1965).

(10) Jackson, S. D., Classical Electrodynamics, 2nd ed.: New York, Wiley and Sons (1975).

(11) King, A. L., Thermophysics: San Francisco, Freeman and Co. (1962).

(12) King, W. R. and C. W. Harrison, Jr., J. Appl. Phys. 39, 9 (1968).

(13) Llewellyn-Jones, F., Ionization and Breakdown in Gases I: New York, Wiley and Sons (1957).

(14) Lorrain, P. and D. Corson, Electromagnetic Fields and Waves, 2nd ed.: San Francisco (1962).

(15) Mass. Institute of Technology Radiation Laboratory Series, Principals of Microwave Circuits: Boston, Boston Technological Lithographers (1947).

(16) Mass. Institute of Technology Radiation Laboratory Series, Principals of Microwave Measurements: Boston, Boston Technological Lithographers (1947).

(17) Mass. Institute of Technology Radiation Laboratory Series, Waveguide Handbook: New York, McGraw-Hill (1951).

(18) Matthews, R. K., Dynamic Stratigraphy: Englewood Cliffs, N. J., Prentice-Hall (1974).

(19) McDonald, D. F. and C. J. Benning, Rev. Sci. Instr. 36, 4 (1965).

(20) The Microwave Engineers' Handbook and Buyers Guide: Dedham, Mass., Horizon House (1966).

(21) Papoulis, A., The Fourier Integral and its Applications: New York, McGraw-Hill (1962).

(22) Pulfrey, D. L., Rev. Sci. Instr.

(23) Seismic Stratigraphy: Tulsa, American Association of Petroleum Geologists (1977).

(24) Southworth, G. C., Principals and Applications of Waveguide Transmission: New York, Van Nostrand Co. (1950).

(25) Spiegel, M. R., Advanced Mathematics for Engineers and Scientists; Schaums Outline Series: New York, McGraw-Hill (1971).

(26) Von Hippel, Dielectrics and Waves: Cambridge, Mass., M.I.T. Press (1954).

(27) Waldron, R. A., Theory of Guided Electromagnetic Waves: New York, Van-Nostrand (1970).

APPENDIX

DERIVATION OF COAXIAL WAVEGUIDE MODES

Assuming a coaxial waveguide as described in Figure 3, the allowed modes of propagation, in particular the E_{oo} transmission line mode, will be derived.

Due to the cylindrical geometry of the guide it is convenient to assume a propagating field of the form:

$$\vec{E}(r,\theta,z,t) = \vec{E}'(r,\theta)e^{ikz-i\omega t}$$

$$\vec{B}(r,\theta,z,t) = \vec{B}'(r,\theta)e^{ikz-i\omega t} .$$

It is also useful to separate the fields into components transverse and parallel to the $\hat{z}$ axis:

$$\vec{E} = \vec{E}_t + \vec{E}_z$$

$$\vec{B} = \vec{B}_t + \vec{B}_z$$

Likewise, the Laplacian operator may be similarly divided;

$$\vec{\nabla}^2(r,\theta,z) = \vec{\nabla}_t^{\,2}(r,\theta) + \vec{\nabla}_z^{\,2}(z)$$

or

$$\vec{\nabla}^2(r,\theta,z) = \vec{\nabla}_t^{\,2}(r,\theta,) + \partial^2/\partial z^2\ \hat{z}$$

Substituting the above expressions into Maxwell's curl equations:

$$\vec{\nabla} x \vec{E} = \frac{i\omega \vec{B}}{c} = -\frac{1}{c}\frac{\partial \vec{B}}{\partial t}$$

$$\vec{\nabla} x \vec{B} = -\frac{i\omega\mu\epsilon}{c}\vec{E} = \frac{\epsilon_\mu}{c}\frac{d\vec{E}}{dt}$$

yields;

$$\vec{\nabla}_t x \vec{E}_t + \vec{\nabla}_t x \vec{E}_z + \hat{z} \times \frac{\partial \vec{E}_t}{\partial z} = \frac{i\omega}{c}\vec{B}_t + \frac{i\omega}{c}\vec{B}_z$$

$$\vec{\nabla}_t x \vec{B}_t + \vec{\nabla}_t x \vec{B}_z + \hat{z} \times \frac{\partial \vec{B}_t}{\partial z} = -\frac{i\omega\mu\epsilon}{c}\vec{E}_t - \frac{i\omega\mu\epsilon}{c}\vec{E}z$$

These two expressions may be divided into four equations each containing only longitudinal or transverse components;

$$\vec{\nabla}_t x \vec{E}_t = \frac{i\omega}{c}\vec{B}_t$$

$$\vec{\nabla}_t x \vec{B}_t = -\frac{i\omega\mu\epsilon}{c}\vec{E}_t$$

$$-\hat{z} \times \vec{\nabla}_t E_z + \hat{z} \times \frac{\partial \vec{E}_t}{\partial z} = \frac{i\omega}{c}\vec{B}_t$$

$$-\hat{z} \times \vec{\nabla}_t B_z + \hat{z} \times \frac{\partial \vec{B}_t}{\partial z} = -\frac{i\omega\mu\epsilon}{c}\vec{E}_t$$

From these equations, a propagating wave equation in terms of only the $\hat{z}$ field components may be derived. This is accomplished by operating on the third equation by $(\hat{z} \times \frac{\partial}{\partial z})$ and adding it to the fourth for a wave equation in terms of $\vec{B}_z$, $(\hat{z} \times \frac{\partial}{\partial z})$ is operated on the fourth equation and added to the third;

$$-\frac{i\omega\mu\epsilon}{c}\hat{z} \times \frac{\partial \vec{E}_t}{\partial z} - \frac{\epsilon\mu\omega^2}{c^2}\vec{B}_t + \frac{i\omega\mu\epsilon}{c}\hat{z} \times \vec{\nabla}_t E_z = 0$$

$$\frac{i\omega\mu\varepsilon}{c}\,\hat{z}\times\frac{\partial\vec{E}_t}{\partial z}-\frac{\partial^2\vec{B}_t}{\partial z^2}+\vec{\nabla}_t B_z=0$$

Adding the two;

$$\vec{\nabla}_t\frac{\partial B_z}{\partial z}+\frac{i\omega\mu\varepsilon}{c}\,\hat{z}\times\vec{\nabla}_t E_z-\left\{\frac{\mu\varepsilon\omega^2}{c^2}-\frac{\partial^2}{\partial z^2}\right\}\vec{B}_t=0$$

and since

$$\frac{\partial^2}{\partial z^2}\vec{B}_t=-k^2\vec{B}_t$$

$$\vec{\nabla}_t\frac{\partial B_z}{\partial z}+\frac{i\omega\mu\varepsilon}{c}\,\hat{z}\times\vec{\nabla}_t E_z-\gamma^2\vec{B}_t=0$$

where

$$\gamma^2=\frac{\mu\varepsilon\omega^2}{c^2}+k^2\,.$$

The above expression may be used to derive the transverse field configuration in the guide in terms of E_z and B_z, however, this will be done shortly. In order to obtain the wave equation in terms of $\vec{E}_z$ it is necessary to operate on the above by $(\vec{\nabla}_t\times)$. This yields;

$$\gamma^2\vec{\nabla}_t\times\vec{B}_t+\frac{\partial}{\partial z}\left(\vec{\nabla}_t\times\vec{\nabla}_t B_z\right)+\frac{i\omega\mu\varepsilon}{c}\,\vec{\nabla}_t\times\hat{z}\times\vec{\nabla}_t E_z=0$$

since it was previously shown that;

$$\vec{\nabla}_t\times\vec{B}_t=-\frac{i\omega\mu\varepsilon}{c}\,\vec{E}_t\,.$$

The equation reduces to;

$$-\frac{i\omega\mu\varepsilon}{c}\gamma^2\vec{E}_z + \frac{i\omega\mu\varepsilon}{c}\nabla_t^2\vec{E}_z = 0$$

and further to;

$$\{\nabla_t^2 - \gamma^2\}\vec{E}_z = 0$$

In a completely analogous manner a wave equation in terms of $\vec{B}_z$ could have been derived.

$$\{\nabla_t^2 - \gamma^2\}\vec{B}_z = 0$$

The Transverse Field Components

The transverse fields may be written in terms of $\vec{E}_z$ and $\vec{B}_z$. The derivation begins with equation,

$$\gamma^2\vec{B}_t = \frac{i\omega\mu\varepsilon}{c}\hat{z} \times \vec{\nabla}_t E_z + ik\vec{\nabla}_t B_t$$

and likewise,

$$\gamma^2\vec{E}_t = \frac{i\omega}{c}\hat{z} \times \vec{\nabla}_t B_z - ik\vec{\nabla}_t E_t$$

The Laplace operator in cylinderical coordinates is:

$$\vec{\nabla}_t = \frac{\partial}{\partial r}\hat{r} + \frac{1}{r}\frac{\partial}{\partial\theta}\hat{\theta}$$

and $\vec{z} \times \vec{\nabla}_t$ may be written as

$$\hat{z} \times \vec{\nabla}_t = \frac{\partial}{\partial r}\hat{\theta} - \frac{1}{r}\frac{\partial}{\partial\theta}\hat{r}$$

Substituting these expressions for the operators into the above two

equations yields

$$\gamma^2 \vec{B}_t = \frac{i\omega\mu\varepsilon}{c} \left\{\frac{\partial}{\partial r} E_z \hat{\theta} - \frac{1}{r}\frac{\partial}{\partial \theta} E_z \hat{r}\right\} + ik \left\{\frac{\partial}{\partial r} B_t \hat{r} + \frac{1}{r}\frac{\partial}{\partial \theta} B_t \hat{\theta}\right\}$$

$$\gamma^2 \vec{E}_t = \frac{i\omega}{c} \left\{\frac{\partial}{\partial r} B_z \hat{\theta} - \frac{1}{r}\frac{\partial}{\partial \theta} B_z \hat{r}\right\} - ik \left\{\frac{\partial}{\partial r} E_t \hat{r} + \frac{1}{r}\frac{\partial}{\partial \theta} E_t \hat{\theta}\right\}$$

From these two vector expressions, four transverse components may be obtained

$$B_r = \frac{ik}{\gamma^2}\frac{\partial B_z}{\partial r} - \frac{i\omega\mu\varepsilon}{\gamma^2 c}\frac{1}{r}\frac{\partial E_z}{\partial \theta}$$

$$E_r = \frac{ik}{\gamma^2}\frac{\partial E_z}{\partial r} + \frac{i\omega}{\gamma^2 c}\frac{1}{r}\frac{\partial B_z}{\partial \theta}$$

$$B_\theta = \frac{ik}{\gamma^2 r}\frac{\partial B_z}{\partial \theta} + \frac{i\omega\mu\varepsilon}{\gamma^2 c}\frac{\partial E_z}{\partial r}$$

$$E_\theta = \frac{ik}{\gamma^2 r}\frac{\partial E_z}{\partial \theta} - \frac{i\omega}{\gamma^2 c}\frac{1}{r}\frac{\partial B_z}{\partial r}$$

Boundary Conditions

When applying boundary conditions to the coaxial waveguide, it is convenient to divide into two distinct regions. Region 1 is the volume described by r = b, to r = a for all z and θ, and region 2 is, r = o, → a for all z and θ. The wave equations for each region are

$$\left\{\nabla_t^2 + \gamma_1^2\right\}\left\{\begin{matrix} E_{z1} \\ B_{z1} \end{matrix}\right\} = 0$$

$$\left\{\nabla_t^2 + \gamma_2^2\right\}\left\{\begin{matrix} E_{z2} \\ B_{z2} \end{matrix}\right\} = 0$$

The solutions to these differential equations may be obtained by the separation of variables technique, and of the form

$$E_z = \{A'J_p(\gamma r) + B'Y_p(\gamma r)\} \sin p\theta$$

$$B_z = \{C'J_p(\gamma r) + D'Y_p(\gamma r)\} \cos p\theta$$

A', B', C', and D' are constants; $J_p(\gamma r)$ and $Y_p(\gamma r)$ are Bessel and Neumann functions of order p respectively. For region 1 the solutions are:

$$E_{z1} = \{CJ_p(\gamma_1 r) + DY_p(\gamma_1 r)\} \sin p\theta$$

$$B_{z1} = \{FJ_p(\gamma_1 r) + GY_p(\gamma_1 r)\} \cos p\theta$$

and region 2:

$$E_{z2} = \{AJ_p(\gamma_2 r) + A'Y_p(\gamma_2 r)\} \sin p\theta$$

$$B_{z2} = \{BJ_p(\gamma_2 r) + B'Y_p(\gamma_2 r)\} \cos p\theta$$

Since $Y_p(r)$ become infinite at r = o it immediately can be seen that A' and B' must be zero in order for the fields to remain finite. The solutions now reduce to:

$$E_{z2} = \{AJ_p(\gamma_2 r)\} \sin p\theta$$

$$B_{z2} = \{BJ_p(\gamma_2 r)\} \cos p\theta$$

The specific boundary conditions to be applied to the solutions are:

at r = b

$$E_{z1} = E_{z2}$$

$$B_{z1} = B_{z2}$$

$$E_{\theta 1} = E_{\theta 2}$$

$$D_{r1} = D_{r2}$$

at r = a

$$E_{z2} = 0$$

$$E_{\theta 2} = 0$$

Applying these boundary conditions to the solutions; six equations in terms of the six constants; A, B, C, D, F, G can be generated. The eigenvalues of k are the solutions of the characteristic equation formed by equating to zero the determinant of the 6 x 6 coefficient matrix. The determinant this matrix must vanish since the six homogeneous equations must be mutually consistent. The six equations are:

1. $A J_p(\gamma_2 b) - C J_p(\gamma_1 b) - D Y_p(\gamma_1 b) = 0$

2. $B J_p(\gamma_2 b) - F J_p(\gamma_1 b) - G Y_p(\gamma_1 b) = 0$

3. $$A \frac{pk_2 \mu \varepsilon_2 \omega}{\gamma_2^2 cb} J_p(\gamma_2 b) + B \frac{\mu \varepsilon_2 \omega}{\gamma_2^2 c} J_p'(\gamma_2 b) - C \frac{k_1 p}{\gamma_1^2 b} J_p(\gamma_1 b)$$

$$- D \frac{pk_1}{\gamma_1^2 b} Y_p(\gamma_1 b) - F \frac{\mu \varepsilon_1 \omega}{\gamma_1^2 c} J_p'(\gamma_1 b) - G \frac{\mu \varepsilon_1 \omega}{\gamma_1^2 c} Y_p'(\gamma_1 b) = 0$$

$$4.\quad A\frac{pk_2\mu\varepsilon_2^2\omega}{\gamma_2^2 c}J_p'(\gamma_2 b) + B\frac{p\mu\varepsilon_2^2\omega}{\gamma_2^2 cb}J_p(\gamma_2 b) + C\frac{k_1\varepsilon_1}{\gamma_1^2}J_p'(\gamma_1 b)$$

$$+ D\frac{k_1\varepsilon_1}{\gamma_1^2}Y_p'(\gamma_1 b) + F\frac{p\mu\varepsilon_1^2\omega}{\gamma_1^2 cb}J_p(\gamma_1 b) + G\frac{p\mu\varepsilon_1^2\omega}{\gamma_1^2 cb}Y_p(\gamma_1 b) = 0$$

$$5.\quad C\,J_p(\gamma_1 a) + D\,Y_p(\gamma_1 a) = 0$$

$$6.\quad C\frac{k_1 p}{a}J_p(\gamma_1 a) + D\frac{k_1 p}{a}Y_p(\gamma_1 a) + F\frac{\mu\varepsilon_1\omega}{c}J_p(\gamma_1 a)$$

$$+ G\frac{\mu\varepsilon_1\omega}{c}Y_p'(\gamma_1 a) = 0$$

From these six equations, the 6 x 6 coefficient matrix is:

$$\begin{vmatrix} J_p(\gamma_2 b) & 0 & -J_p(\gamma_1 b) \\ 0 & J_p(\gamma_2 b) & 0 \\ \frac{pk_2\mu\varepsilon_2\omega}{\gamma_2^2 cb}J_p(\gamma_2 b) & \frac{\mu\varepsilon_2\omega}{\gamma_2^2 c}J_p'(\gamma_2 b) & -\frac{pk_1}{\gamma_1^2 b}J_p(\gamma_1 b) \\ \frac{pk\mu\varepsilon_2^2\omega}{\gamma_2^2 c}J_p'(\gamma_2 b) & \frac{p\mu\varepsilon_2^2\omega}{\gamma_2^2 cb}J_p(\gamma_2 b) & \frac{k_1\varepsilon_1}{\gamma_1^2}J_p'(\gamma_1 b) \\ 0 & 0 & J_p(\gamma_1 a) \\ 0 & 0 & \frac{pk_1}{a}J_p(\gamma_1 a) \end{vmatrix}$$

$$\begin{vmatrix} -Y_p(\gamma_1 b) & 0 & 0 \\ 0 & -J_p(\gamma_1 b) & -Y_p(\gamma_1 b) \\ -\frac{pk_1}{\gamma_1^2 b} Y_p(\gamma_1 b) & -\frac{\mu\varepsilon_1\omega}{c\gamma_1^2} J_p'(\gamma_1 b) & -\frac{\mu\varepsilon_1\omega}{\gamma_1^2 c} Y_p'(\gamma_1 b) \\ \frac{k_1\varepsilon_1}{\gamma_1^2} Y_p'(\gamma_1 b) & \frac{\mu\varepsilon_1^2\omega p}{\gamma_1^2 cb} J_p(\gamma_1 b) & \frac{\mu\varepsilon_1^2\omega p}{cb\gamma_1^2} Y_p(\gamma_1 b) \\ Y_p(\gamma_1 a) & 0 & 0 \\ \frac{pk_1}{a} Y_p(\gamma_1 a) & \frac{\mu\varepsilon_1\omega}{c} J_p'(\gamma_1 a) & \frac{\mu\varepsilon_1\omega}{c} Y_p'(\gamma_1 a) \end{vmatrix} = 0$$

Upon evaluating the determinant, it is convenient to define a set of smaller determinants as

$$W = \begin{vmatrix} J_p(\gamma_1 a) & Y_p(\gamma_1 a) \\ J_p(\gamma_1 b) & Y_p(\gamma_1 b) \end{vmatrix} \qquad X = \begin{vmatrix} J_p(\gamma_1 a) & Y_p(\gamma_1 a) \\ J_p'(\gamma_1 b) & Y_p'(\gamma_1 b) \end{vmatrix}$$

$$Y = \begin{vmatrix} J_p'(\gamma_1 a) & Y_p'(\gamma_1 a) \\ J_p(\gamma_1 b) & Y_p(\gamma_1 b) \end{vmatrix} \qquad Z = \begin{vmatrix} J_p'(\gamma_1 a) & Y_p'(\gamma_1 a) \\ J_p'(\gamma_1 b) & Y_p'(\gamma_1 b) \end{vmatrix}$$

After much labor, the characteristic equation obtained after equating the determinant to zero is:

$$\left\{\frac{\varepsilon_2}{\varepsilon_1}\gamma_1 J_p'(\gamma_2 b)W - \gamma_2 J_p(\gamma_2 b)X\right\}\left\{\gamma_1 J_p'(\gamma_2 b)Y - \gamma_2 J_p(\gamma_2 b)Z\right\}$$

$$- \frac{p^2 k^2 (\gamma_2^2 - \gamma_1^2)^2}{\varepsilon_1^2 \gamma_2^2 \gamma_1^2 b^2} J_p(\gamma_2 b)WY = 0$$

From the characteristic equation any mode, E_{pq} or H_{pq}, may be found. The subscript q is an integer describing the particular Bessel function root used to solve the equation and p is the order of the Bessel function.

The E_{oo} Mode

For E_{oo} transmission line mode p will be zero, such that the characteristic equation reduces to:

$$\left\{\frac{\varepsilon_2}{\varepsilon_1}\gamma_1 J_o'(\gamma_2 b)W - \gamma_2 J_o(\gamma_2 b)X\right\} = 0$$

From the recurrence formulas for Bessel functions, the derivative of a Bessel function is equivalent to (25):

$$J_n'(x) = \tfrac{1}{2}[J_{n-1}(x) - J_{n+1}(x)]$$

$$Y_n'(x) = \tfrac{1}{2}[Y_{n-1}(x) - Y_{n+1}(x)]$$

thus,

$$J_o'(\gamma_2 b) = -\tfrac{1}{2} J_1(\gamma_2 b)$$

$$Y_o'(\gamma_1 b) = -\tfrac{1}{2} Y_1(\gamma_1 b) .$$

Assuming the waveguide is air-filled, $\varepsilon_1 = 1$ and the characteristic equation becomes:

$$- \varepsilon_2 \frac{\gamma_1}{\gamma_2} J_1(\gamma_2 b) \begin{bmatrix} J_o(\gamma_1 a) & Y_o(\gamma_1 a) \\ J_o(\gamma_1 b) & Y_o(\gamma_1 b) \end{bmatrix} + J_o(\gamma_2 b) \begin{bmatrix} J_o(\gamma_1 a) & Y_o(\gamma_1 a) \\ J_1(\gamma_1 b) & Y_1(\gamma_1 b) \end{bmatrix} = 0$$

The first solution of this expression corresponds to the $E_{01}(H_{01})$ mode, and there is no indication of the E_{oo} mode. However, the E_{oo} mode may be obtained by generalization of the guide (27). In particular, instead of assuming perfect conductors, the inner rod is assumed to be a dielectric, ε_2. As ε_2 becomes totally imaginary, $\varepsilon_2 = i\varepsilon_2$, the inner rod reduces to the perfect case.

Recalling the expressions for the propagation constants:

$$\gamma_1^2 = \frac{\omega^2}{c^2} - k^2$$

$$\gamma_2^2 = \frac{\mu\varepsilon\omega^2}{c^2} - k^2$$

Assuming that γ_1^2 is very close to zero for region 1, in the limit as $\gamma_1 \to 0$ the characteristic equation may be satisfied. For small values of γ_1, the Bessel and Neumann functions reduce to:

$$J_o(\gamma_1 a) \approx 1 \qquad Y_o(\gamma_1 a) \approx \frac{2}{\pi} \ln\left(\frac{\gamma_1 a}{2}\right)$$

$$J_o(\gamma_1 a) \approx \frac{\gamma_1 a}{2} \qquad Y_1(\gamma_1 a) \approx -\frac{2}{\gamma_1 \pi a}$$

with similar expressions for $(\gamma_1 b)$. Substituting these expressions into the characteristic equation:

$$\varepsilon_2 \frac{\gamma_1}{\gamma_2} \frac{2}{\pi} \ln\left(\frac{a}{b}\right) - \frac{J_o(\gamma_2 b)\ 2}{\pi \gamma_1 b} = 0$$

or;

$$\frac{\varepsilon_2 \gamma_1^2}{\gamma_2} = \frac{J_o(\gamma_2 b)}{b J_1(\gamma_2 b)\ \ln(\frac{a}{b})}$$

At the cutoff frequency; $\gamma_2 = \frac{2\pi}{\lambda_2}\sqrt{i\varepsilon_2}$, since k = o. γ_1 may be written as; $\gamma_1 = \frac{2\pi}{\lambda_o}$. The equation now becomes:

$$\frac{\lambda_o}{\lambda_c} = \frac{J_o(\gamma_2)}{\sqrt{i\varepsilon_2}\ (\frac{2\pi b}{\lambda_o})\ J_1(\gamma_2 b)\ \ln(\frac{a}{b})}$$

Replacing $\frac{\lambda_o}{\lambda_c}$ by; $1 - \bar{k}^2$ where $\bar{k}$ is $\sqrt{1 - \frac{\lambda_o}{\lambda_c}}$.

$$1 - \bar{k}^2 = \frac{J_o(\gamma_2 b)}{\sqrt{i\varepsilon_2}\ (\frac{2\pi b}{\lambda_o})\ J_1(\gamma_2 b)\ \ln(\frac{a}{b})}$$

or,

$$1 - \bar{k}^2 = \frac{(1-i)\ J_o(\gamma_1 b)}{\sqrt{2\varepsilon_2}\ (2\pi b/\lambda_o)\ J_1(\gamma_1 b)\ \ln(\frac{a}{b})}$$

In the limit as $\varepsilon_2 \to \infty$, $\bar{k}^2 \to 1$ and the characteristic equation is satisfied. This zeroth solution is the E_{oo} mode. For $\bar{k}^2 = 1$,

$$\bar{k} = \sqrt{1 - \frac{\lambda_o}{\lambda_c}} = 1$$

thus,

$$\frac{\lambda_o}{\lambda_c} = 0 .$$

This corresponds to $\lambda_c = \infty$, and,

$$k = \frac{2\pi}{\lambda_o} = \frac{\omega}{c}$$

The phase velocity is defined as $v_\phi = \frac{\omega}{k}$, which for the E_{oo} mode is:

$$v_\psi = c$$

The group velocity, $v_g = \frac{d\omega}{dk}$, is:

$$v_g = \frac{d\omega}{dk} = c$$

Field Components

The field components may easily be found for the E_{oo} mode by beginning with $B_z \equiv 0$ and $\frac{\partial}{\partial\theta} \equiv 0$. From the expressions for the components:

$$B_r = E_\theta = B_z \equiv 0$$

$$E_r = \frac{ik}{\gamma^2} \frac{\partial E_z}{dr} = \frac{q_\ell}{2\pi r\varepsilon}$$

$$B_\theta = \frac{i\omega\mu\varepsilon}{c\gamma^2} \frac{\partial E_z}{dr} = \frac{q_\ell\ \omega}{2\pi r\gamma}$$

which can be seen to be identical to the electrostatic case.

VITA - 2

Steven Michael Shope

Candidate for the Degree of

Master of Science

Thesis: THE PROPAGATION OF ELECTROMAGNETIC WAVES THROUGH STRATIFIED TERRESTRIAL MEDIA

Major Field: Physics

Biographical:

Personal Data: Born the 8th of April, 1953, in Pittsburgh, Pennsylvania.

Education: Graduated from Central High School, Martinsburg, Pennsylvania, in May, 1971; received Bachelor of Arts degree in Physics from Lycoming College, Williamsport, Pennsylvania, in 1978; completed the requirements for the Master of Science degree at Oklahoma State University, December, 1978.

Professional Experience: Work-study Engineer, Litton Industries, Electron Tube Division, 1974-75; Continential Oil Company, Seismograph Observer, 1975-78; Graduate Teaching Assistant, Department of Physics, Oklahoma State University, 1976-78; Graduate Research Assistant, Department of Physics, Oklahoma State University, 1978.